ADVANCED ENERGY MATERIALS
www.advenergymat.de

Intrinsic Mechanical Parameters and their Characterization in Solid-State Lithium Batteries

Shuai Hao, Qianyi Zhang, Xiangkang Kong, Zhaoxiang Wang, Xue-Ping Gao, and Paul R. Shearing**

The most critical failures in solid-state batteries, including interfacial detachment, cracks, and dendrite growth are coupled with or fundamentally belong to a class of overarching phenomena that may be broadly defined as mechanical processes. However, current research on mechanical processes is far from sufficient, and is in its infancy compared with studies of improving electrolyte ionic transportation and electrochemical stabilities. Even the physical significance of many mechanical parameters has not been clarified in this field and the corresponding characterization methods have not yet been widely established. Herein, this review focuses on the intrinsic mechanical parameters associated with the design and operation of solid-state batteries and their characterization. Beginning with an overview of mechanical processes, key concepts in the context of solid-state batteries (SSB) are defined. Next, the various characterization methods that have been applied to SSBs are described in detail, and the key results are reviewed. Additional methods applied in orthogonal areas are also included to emphasize the possible translational impact on the solid-state battery field. Finally, perspectives on the challenges and development trends in mechanical characterization are proposed for further development in solid-state batteries.

1. Introduction

Solid-state batteries (SSB) are one of the most promising candidates for next-generation batteries and are at the center of major, international research efforts in academia and industry. Many of the existing obstacles in solid-state battery commercialization arise from their mechanical properties, an area of growing research but one that remains comparatively under-studied. In SSB operation, the mechanical behavior has equal importance to the electrochemical and chemical behavior, and therefore more fundamental investigations are required to better elucidate these important processes.

In the traditional lithium-ion battery, mechanical forces can be largely alleviated by the liquid electrolyte, especially in a single cell. By contrast, in the solid-state configuration, the mechanical forces and processes become much more obvious and non-negligible owing to the rigid nature of the solid-solid interfaces and their constrained volume. Many solid electrolytes are inflexible, like the oxides (eg. $Li_7La_3Zr_2O_{12}$ including doping phases (LLZO), $Li_{1.3}Al_{0.3}Ti_{1.7}(PO_4)_3$ (LATP), etc.) and sulfides (eg. Li_2S-P_2S_5 in different ratios (LPS), $Li_{10}GeP_2S_{12}$ (LGPS), etc.). Even polymer-based and composite solid electrolytes display reduced flexibility compared to conventional Li-ion separators immersed in liquid electrolytes. The introduction of solid electrolytes brings several new solid-solid interfaces with electrodes and current collectors, in replacement of the solid-liquid ones

S. Hao, Q. Zhang, X. Kong, X.-P. Gao
Institute of New Energy Material Chemistry
School of Materials Science and Engineering
Nankai University
Tianjin 300350, China
E-mail: haoshuai@nankai.edu.cn

Z. Wang
Beijing National Laboratory for Condensed Matter Physics
Institute of Physics
Chinese Academy of Sciences
Beijing 100190, China

The ORCID identification number(s) for the author(s) of this article can be found under https://doi.org/10.1002/aenm.202404384

© 2024 The Author(s). Advanced Energy Materials published by Wiley-VCH GmbH. This is an open access article under the terms of the Creative Commons Attribution License, which permits use, distribution and reproduction in any medium, provided the original work is properly cited.

DOI: 10.1002/aenm.202404384

Z. Wang
School of Physical Sciences
University of Chinese Academy of Sciences
Beijing 100049, China

Z. Wang
College of Materials Science and Opto-Electronic Technology
University of Chinese Academy of Sciences
Beijing 100049, China

P. R. Shearing
The Faraday Institution
Quad One
Harwell Science and Innovation Campus
Didcot OX11 0RA, UK
E-mail: paul.shearing@eng.ox.ac.uk

P. R. Shearing
The ZERO Institute
University of Oxford
Holywell House, Oxford OX2 0ES, UK

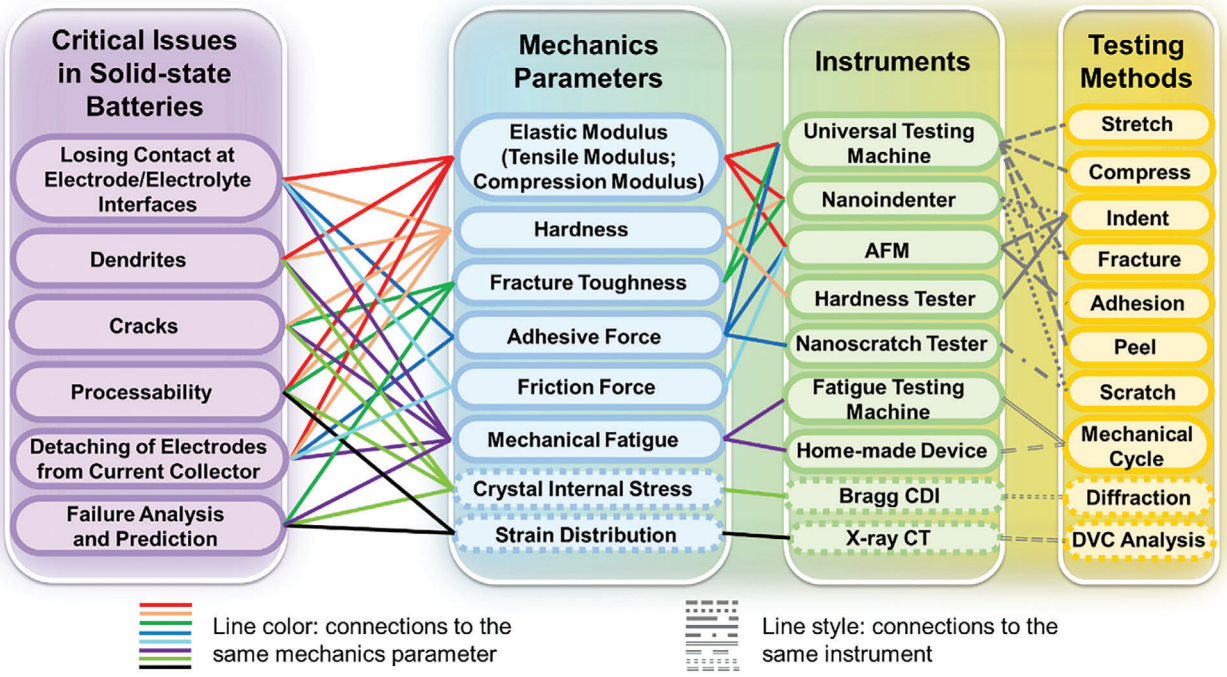


Figure 1. The summary of mechanical parameters, and their correlations to the critical issues in solid-state batteries, instruments, and corresponding testing methods.

in the liquid electrolyte systems. The solid-solid contact is easily influenced by the mechanical environment and can degrade the electrochemical performance in turn. Furthermore, pursuing higher capacities in solid-state batteries results in larger volume expansion and shrinkage in electrode materials, as more lithium-ions are inserted/extracted during charging/discharging. This induces further stress and strain in cells. Additionally, the mechanical properties of solid electrolytes and electrodes also give rise to new challenges during processing and cell assembly, especially in mass production.

In spite of this, the investigations and understanding of the mechanical processes and properties in solid-state batteries are still at a comparatively early stage, though they are attracting increasing attention.[1] Previously, significant efforts in solid-state batteries were paid to material synthesis and modification, electrochemical performance, and crystallographic structure. While, the detailed mechanical properties and processes, including elasticity, plasticity, fracture, adhesion, friction, and mechanical fatigue, have not been fully studied yet.

The fundamental mechanics of solid-state batteries remain unclear, the first step in their further elucidation is largely determined by the available mechanical characterization tools which set the scope of studies. Whilst the portfolio of tools that have been applied within SSB development remains relatively limited, many mechanical measurement methods have previously been developed and applied in the fields of building materials, manufacturing, and aerospace, which provide orthogonal expertise to the lithium battery field. There is an opportunity for the systematic combination of these mechanical measurements alongside more established electro/chemical tools to enhance our understanding of SSBs.

Herein, this review focuses on the intrinsic mechanical parameters in solid-state batteries and characterization methods that can be applied to improve this understanding. First, we introduce and review the key mechanical processes in solid-state batteries, as well as their different causes and influences on the electrochemical performance. Next, the characterization methods for each parameter are systematically categorized and described, and their successful applications in solid-state batteries are summarized. Some methods that have not yet been used in the solid-state battery but have translation potential are also included as a reference. Finally, perspectives are proposed on the further development of mechanical characterization for exploring solid-state batteries. Overall, the mechanical parameters and their correlations to the critical issues in solid-state batteries, are summarized in **Figure 1** alongside corresponding instrument and testing methods.

2. Mechanical Processes in Solid-State Batteries

The different mechanical processes in solid-state batteries, localized in different areas of the cell, are illustrated in **Figure 2**. Key processes include: losing contact at the electrode/electrolyte interfaces, detachment from current collectors (Cu or Al foils), void generation at interfaces, crack propagation inside solid electrolytes, and the application of external pressure.

These processes are induced and influenced by a multitude of electrochemical, chemical, and external factors. First, the volume changes (expansion or shrinkage) in cathodes and anodes due to the lithiation or de-lithiation have a profound effect on the solid/solid interface between electrode and electrolyte. The second major factor is the external pressure applied to the whole

© 2024 The Author(s). Advanced Energy Materials published by Wiley-VCH GmbH

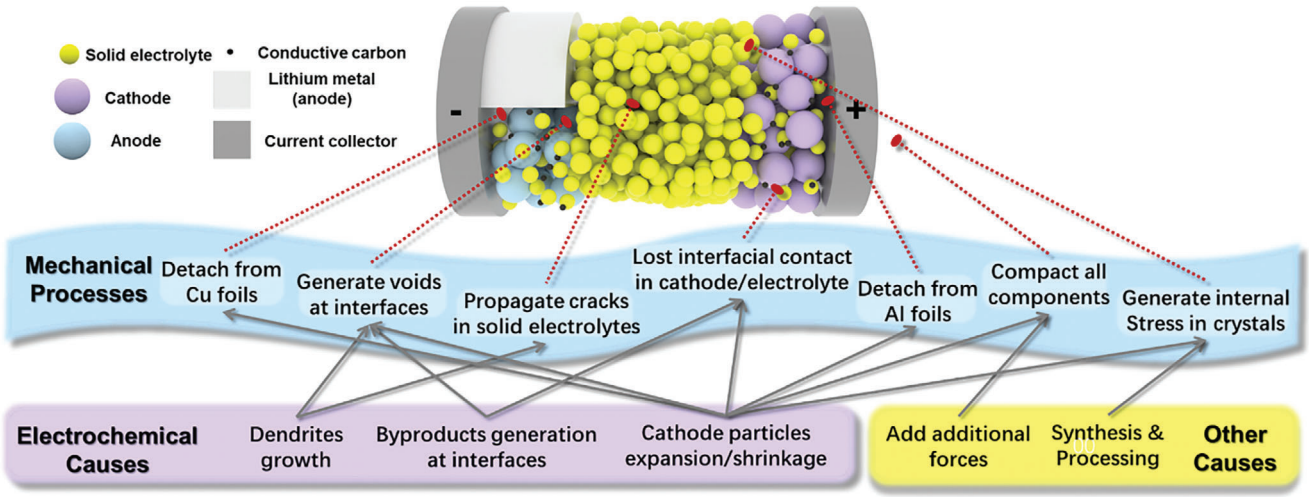


Figure 2. Schematic of mechanical processes and their causes in solid-state batteries.

packaged cell and/or module, which is inevitable in both a single cell and large battery packs. Moreover, dendrites and byproducts that are generated at the interfaces can also add local pressure.

These mechanical effects have a significant influence on further electrochemical processes, such as impedance increasing, uneven distribution of the lithium-ion flux and the electrical field, fast decay in capacities, and short circuits. As a whole, the mechanical processes are intimately coupled with the electrochemical ones and their interplay will be discussed in the following sections.

2.1. Cathode

The extraction or insertion of lithium ions from the cathode materials leads to volume changes, which happen in both liquid and solid electrolytes. The magnitude of the volume change is largely related to the reaction mechanism, and generally speaking, cathode materials that have intercalation reactions usually show relatively small volume changes, while those relying on conversion reactions are generally much larger. $LiCoO_2$, as one of the most widely used cathode materials, de/intercalates lithium ions into the α-$NaFeO_2$ layered structure. The cell volume increases by 1.9% when 0.5 mol Li-ions are extracted from the lattice.[2] Sulfur is a typical conversion-type cathode and transforms into Li_2S after lithiation with an associated volume change of ca. 79%.[3] Another series of layered cathodes are ternary $LiNi_xMn_yCo_zO_2$ (x+y+z = 1, abbreviated as NMC). As the Ni ratio increases, the extent of volume change increases. When charged (de-intercalated) to 4.4 V, the NMC111, NMC622, and NMC811 materials shrink by 3.4%, 5.2%, and 7.8%, respectively.[4,5] $LiFePO_4$ mainly shows a two-phase reaction mechanism with a phase transition between $LiFePO_4$ and $FePO_4$. Its volume correspondingly shrinks by 6.5%.[2]

The volume expansion/shrinkage in the densified solid-state battery leads to internal stresses. As a consequence, the intimately contacted cathode particles, solid electrolytes, and conductive additives inside cathode composites can detach[6] and the layers of cathode electrodes can delaminate from the current collector foils.[7]

As the dynamics of lithium-ion transport are usually more sluggish in solid-state batteries compared with liquid electrolyte systems, the inhomogeneity in de-/lithiation processes becomes more severe through the plane direction of the electrodes.[8] The electrochemical reactions begin at the cathode/electrolyte interfaces and gradually proceed toward the cathode/current collector interfaces.[9] These factors further complicate the effects of local volume changes and induce heterogeneity of local stresses.

2.2. Anode

Anode materials also demonstrate volume changes during de-/lithiation, which can be alleviated to a large extent in the liquid electrolyte systems. The graphite expands 13.1% in volume after it is fully lithiated to LiC_6.[10] The zero-strain material $Li_4Ti_5O_{12}$ has a minor volume change of 0.2%.[11] In contrast, the anode materials with alloying reactions usually undergo a huge volume expansion, such as Si, In, and Al, which expand by 310%,[12] 105.6%,[13] and 100%,[14] respectively.

Where metallic electrodes are utilized, another important issue is the inhomogeneous deposition and stripping of lithium which can leave lithium dendrites or voids on anode surfaces.[15,16] The surface heterogeneity can deteriorate further in the following cycles, inducing local stresses and making both electronic and force fields more inhomogeneous.

2.3. Solid Electrolytes

Limited by the synthesis and assembling methods, solid electrolytes will always contain surface heterogeneities or defects that may act as the nucleation points for lithium deposition. The growing amount of locally deposited lithium induces stresses in those regions and the surface unevenness deteriorates further at the anode/electrolyte interfaces. When the stress accumulates at the tips of the flaws, it can fracture the bulk of solid

© 2024 The Author(s). Advanced Energy Materials published by Wiley-VCH GmbH

electrolytes.[17] For inorganic solid electrolytes, like LLZO and LPS, cracks originate and propagate thereafter, resulting in a fractured electrolyte.[18,19] For organic electrolytes, like polyethylene oxide (PEO)-based polymer, the polymer films can be pierced with some deformations.[20] The concentrated stresses are released to a great extent at this time. Then, with more lithium depositing into the cracks or holes, stresses will continue growing and forcing the cracks to be widened.[21] These mechanical processes are coupled with the electrochemical reactions and finally result in a sudden short circuit in the cells, which remains a critical problem in solid-state batteries.

Additionally, some solid electrolytes have side reactions with cathode or anode materials, which results in byproducts at those interfaces which can disrupt the intimate contact at the interfaces. The influence of these behaviors on mechanical issues remains poorly understood, and under-studied compared to chemical or electrochemical instabilities of electrolytes and ionic and electronic conductivities of the byproducts.

The complex stress/strain behavior produced in cathodes, anodes, and solid electrolytes, causes different degrees of expansion or shrinkage in each component of the cells due to their different mechanical properties. Therefore, maintaining the cathode/electrolyte and anode/electrolyte interfaces, especially after electrochemical cycles, is a significant challenge that is currently hindering SSB commercialization.

2.4. External Pressures

Adding external pressure to the whole solid-state battery is an effective way to maintain interfaces in close contact.[22] Therefore, a high stack pressure is commonly used in cell assembling; usually several tons (equivalent to hundreds of MPa) for oxide and sulfide solid electrolytes, and relatively smaller values (several MPa) for polymer and composite solid electrolytes. It is worth noting that this pressure has a beneficial effect when it is in a certain range, forcing on all parts of the batteries without fracturing them. If the pressure goes higher than the maximum value that the electrolytes and electrodes can withstand, the solid electrolytes or electrodes could crack before any electrochemical cycles.[23]

Besides the stack pressure in assembling, additional pressures are also applied by kinds of bespoke devices to maintain the pressures during electrochemical cycles. Also, they significantly influence the performance of solid-state batteries, which will be discussed further in Section 3.8.

2.5. Synthesis & Processing Processes

Synthesizing and processing solid electrolytes and electrodes can cause internal stresses in their crystals. Usually, these microscopic stresses are induced by macroscopic mechanical processes, chemical reactions, and thermal changes, which may happen simultaneously during synthesis and processing. On the other hand, once the internal stresses are formed, they influence the macroscopic mechanical properties in turn. In solid-state batteries, the internal stresses in solid electrolytes or electrodes have effects on preventing lithium dendrites.[24,25] Besides, processes including winding, calendaring, stacking, and so on (during which various forces are induced in the solid-state batteries) also mandate good mechanical properties for the solid electrolyte and electrodes to withstand all these forces and deformations.

2.6. Mechanical Abusive Loading

Except for the normal processes mentioned above, mechanical abusive loading needs attention, especially in practical cases in the real world. All battery configurations can be subjected to some unexpected mechanical forces in storage or in operation. These forces correspond to various deformations, including bending, indentation, compression, twisting, and so on. For lithium-ion batteries using liquid electrolytes, these mechanical forces may cause a short circuit, and resulting catastrophic failures have been reported and are the subject of many investigations.[26–29] As solid-state batteries progress toward real-world deployment, the risks associated with mechanical abusive loading should not be ignored which highlights the importance of mechanical characterization and understanding both in underpinning fundamental studies, as well as in certification testing.

3. Mechanics Parameters and Characterizations in SSB

The complexity and importance of mechanical processes in solid-state batteries call for comprehensive and exhaustive investigations. In mechanics, a bulk material can undergo elastic deformation, plastic deformation, and fracture; the solid/solid interfaces have adhesion and friction behaviors; repeated mechanical processes can cause fatigue or failure of a whole component. Correspondingly, mechanical parameters describe these mechanical processes and properties from different perspectives, which must be carefully described and distinguished in the context of solid-state batteries. Additionally, the broad portfolio of available mechanical characterization methods has not been extensively applied in the lithium battery field, compared with the fields of manufacturing, building, aerospace, and so on.

In the following sections, the definitions of each mechanical parameter are clarified first. Then, the test methodology, including the corresponding testing instruments is described, followed by application examples in the field of solid-state batteries. Meanwhile, some test approaches used in liquid electrolyte systems and orthogonal areas, are also considered. The mechanical parameters in evaluating solid-state batteries and corresponding characterization methods are summarized in **Figure 3**. Then, the following figures (**Figures 4–10**) in this section are grouped by the testing instrument.

3.1. Tensile Modulus (E_T)

Definition: In the range of elastic deformation, the elastic modulus (E) is defined as the ratio of stress and the corresponding strain, describing the object's resistance to being deformed elastically. Based on the directions of imposed stresses, it is divided into different types: tensile modulus (tensile stress), compression modulus (compression stress), shear modulus (shear

© 2024 The Author(s). Advanced Energy Materials published by Wiley-VCH GmbH

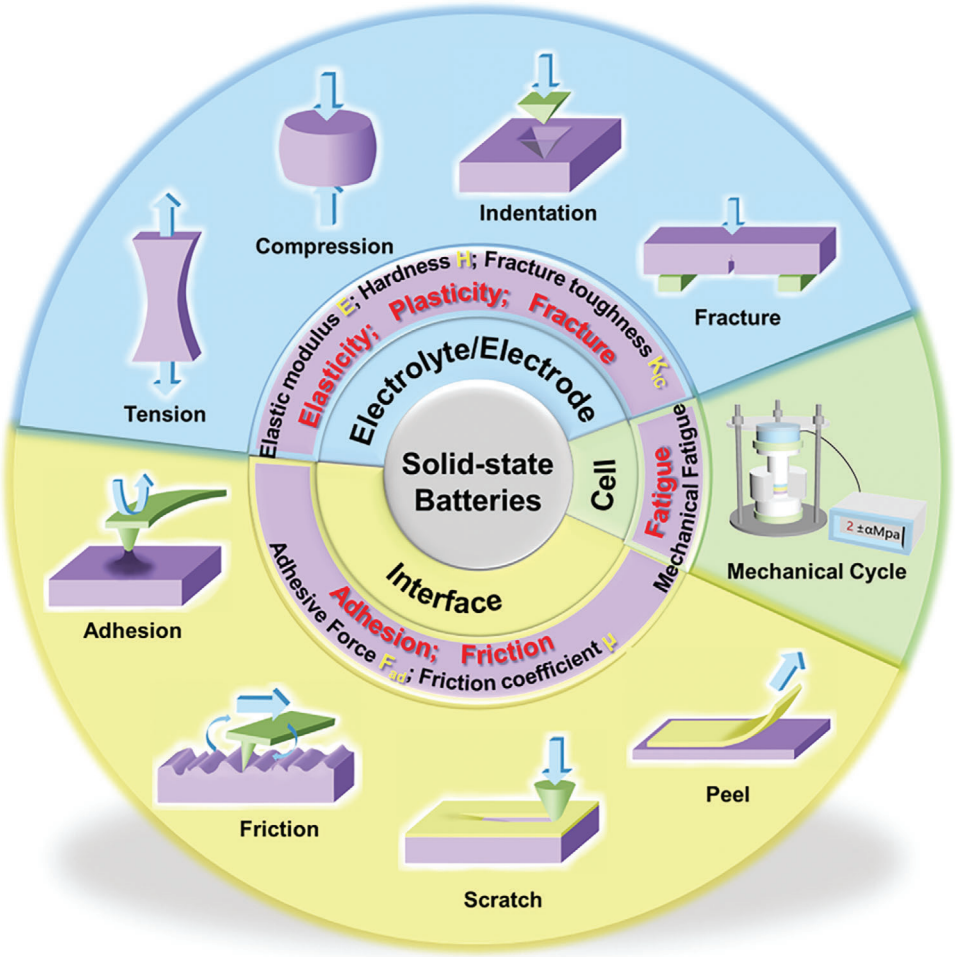


Figure 3. The mechanical parameters and corresponding characterization methods used in solid-state batteries.

stress), and so on. For the sake of clarity, we discuss the tensile modulus in this section while the compression and shear moduli are discussed in Sections 3.2 and 3.3, respectively.

The tensile modulus (E_T) quantifies the ratio of tensile stress (σ, force per unit area) to normal strain (ε, proportional deformation) as $E_T = \sigma/\varepsilon$, within the scope of Hooke's law and belongs to the wider definition of Young's modulus which is widely used in engineering. The tensile strength is defined as the maximum stress that the sample can sustain during the tensile process.

Measurement and Application Examples in SSB: The universal testing machine (Figure 3a) is commonly used to stretch samples and the tensile modulus is calculated from the obtained stress–strain curves. In the area of solid-state batteries, it is applied to measure the stretchability of polymer electrolytes or composite electrolytes and their changes as a function of adjusting the solid electrolyte compositions.[30–43] For example, Tang et al.[32] added vermiculite sheets (VS) into a PEO-based polymer electrolyte with LiTFSI as salts, and found the tensile modulus was increased from 6.8 to 13.1 MPa because the 2D structure of vermiculite sheets with a high aspect ratio large effective interfaces with the polymer matrix (Figure 4b). Pan et al.,[41] prepared polyvinyl formal (PVFM) based polymer electrolytes with different contents of PEO blending. With PEO ratios increasing from 10%, 20% to 30%, the tensile strength of electrolytes was dramatically enhanced from 4.33, 6.80 to 12.81 MPa, which is even higher than the strength of the PVFM-based dense membrane itself (Figure 4c). This was attributed to the change of crystallization states in the PVFM/PEO blend membrane. Meanwhile, the elongation at break values decreased correspondingly, because the PEO crystallites inhibited the orientation of PVFM chains under external tension. Overall, adding additives (such as SiO_2,[30] MnO_2 nanosheet,[31] TiO_2,[33] graphene,[36,37,42] $LiClO_4$,[38] succinonitrile,[39] bacterial cellulose)[40] and adjusting the ratio of polymer components[34,35,43] have been demonstrated as two effective methods to adjust the Yong's modulus and tensile strength in polymer or composite electrolytes, which guides further modifications of these mechanical properties. Besides, cyclic tension can induce changes in tensile properties, which can be tested as well, as discussed in Section 3.8.

Taking both mechanical and electrochemical processes into consideration, the tensile modulus and tensile strength of solid electrolytes affect the lithium dendrite growth, interfacial contact as well as machinability for mass production and cell assembly.

© 2024 The Author(s). Advanced Energy Materials published by Wiley-VCH GmbH

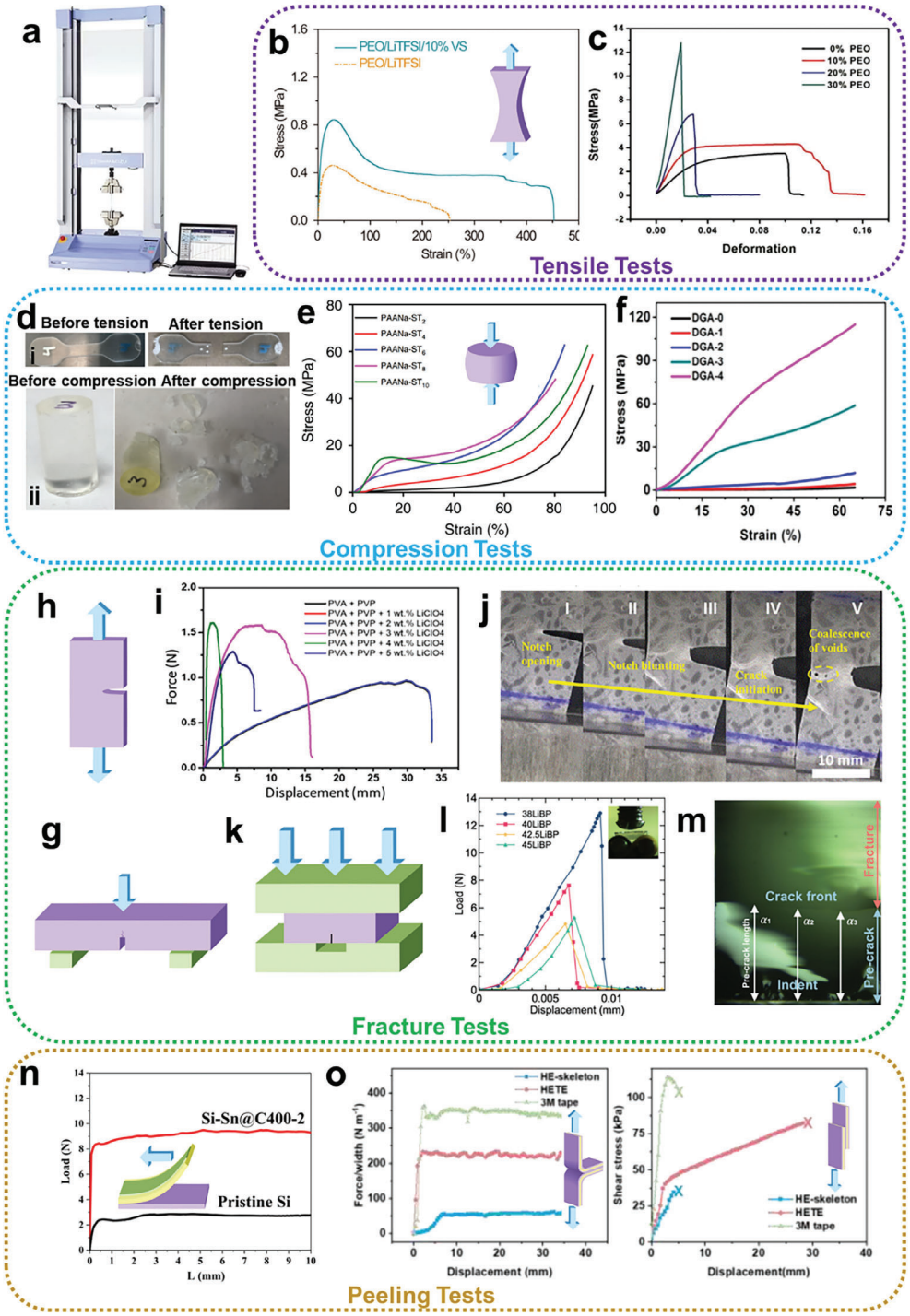


Figure 4. Collection of mechanical tests on the universal testing machine. a) Photo of the universal testing machine; (b,c) Stress–strain curves of the solid polymer electrolyte PEO/LiTFSI-VS. Adapted with permission.[32] Copyright 2018, Wiley-VCH (b) and PVFM-PEO. Reproduced with permission.[41] Copyright 2015, Wiley-VCH (c) under tensile test; d) Casting polymer electrolytes for (i) tensile and (ii) compression tests; e,f) Compressive curves of the crystallohydrate-polymer composite electrolyte. Adapted with permission.[44] Copyright 2020, Springer-Nature (e) and solid electrolyte filled graphene. Reproduced with permission.[45] Copyright 2018, Elsevier (f); g,h) Schematic of the notched-beam method (g) and the single-edge notched tension method (h) for fracture tests; i,j) Force-displacement curves (i) and optical images (j) of a PVA/PVP/$LiClO_4$ polymer electrolyte. Reprduced with permission.[46] Copyright 2022, Wiley-VCH; k) Schematic of the pre-cracking method for fracture tests; l,m) Load-displacement curves (l) and corresponding post-fractured specimen (m) of LBP electrolyte. Reproduced with permission[47] Copyright 2023, Elsevier; n) The peeling test curves of two anode materials and schematic image (inset). Adapted with permission[48] Copyright 2021, ACS; o) Force/width-displacement curves for 180-degree peeling tests (left) and shear stress-displacement curves for lap-shear tests (right) on PEO-based polymer electrolyte. Adapted with permission[49] Copyright 2023, Wiley-VCH, with schematic images in insets.

© 2024 The Author(s). Advanced Energy Materials published by Wiley-VCH GmbH

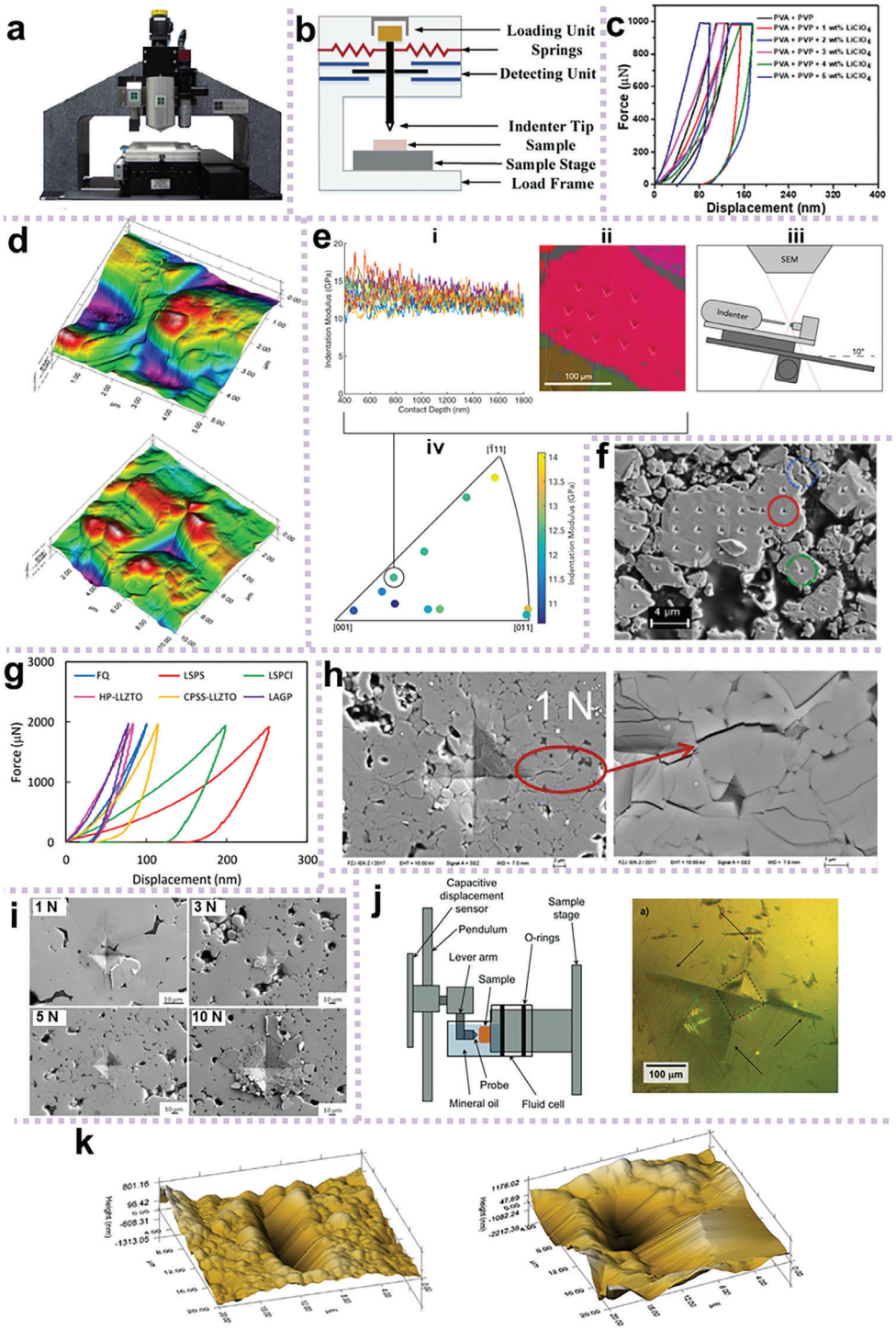


Figure 5. Collection of mechanical tests on nanoindenter. a,b) Photo (a) and schematic images (b) of a nanoindenter instrument. Reproduced according to the terms of the CC-BY license.[55] Copyright 2018, The Authors, published by MDPI; c,d) Force-displacement curves (c) and 3D images (d) of PVA/PVP polymer electrolyte (before (top) and after (bottom) indentation). Adapted with permission[46] Copyright 2022, Wiley-VCH; e) A nanoindenter coupled with EBSD in detecting the elastic modulus of lithium metal. Reproduced with permission[53] Copyright 2022, Elsevier; f) SEM image of nanoindentation tests on $LiMn_2O_4$ particles. Reproduced with permission[54] Copyright 2014, Elsevier; g) Force-displacement curves of nanoindentation on different sulfide and oxide solid electrolytes. Reproduced with permission[56] Copyright 2021, Elsevier; h,i) SEM images of indentation marks for KIC on $Na_{1+2x}Al_xY_xZr_{2-2x}(PO_4)_3$ electrolyte. Reproduced with permission[57] Copyright 2019, Elsevier; (h) and LLZO with different loads. Reproduced with permissioin[51] Copyright 2019, Springer Nature (i); j) Schematic of nanoindenter used to immerse the Li_2S-P_2S_5 electrolyte (left) and the resulting fracture image (right). Adapted with permission[58] Copyright 2017, Wiley-VCH; k) 3D images of the nanoscratch impressions on Si electrodes ((left) Si@starch/PEG and (right) Si@PVDF). Reproduced with permission[59] Copyright 2020, ACS.

© 2024 The Author(s). Advanced Energy Materials published by Wiley-VCH GmbH

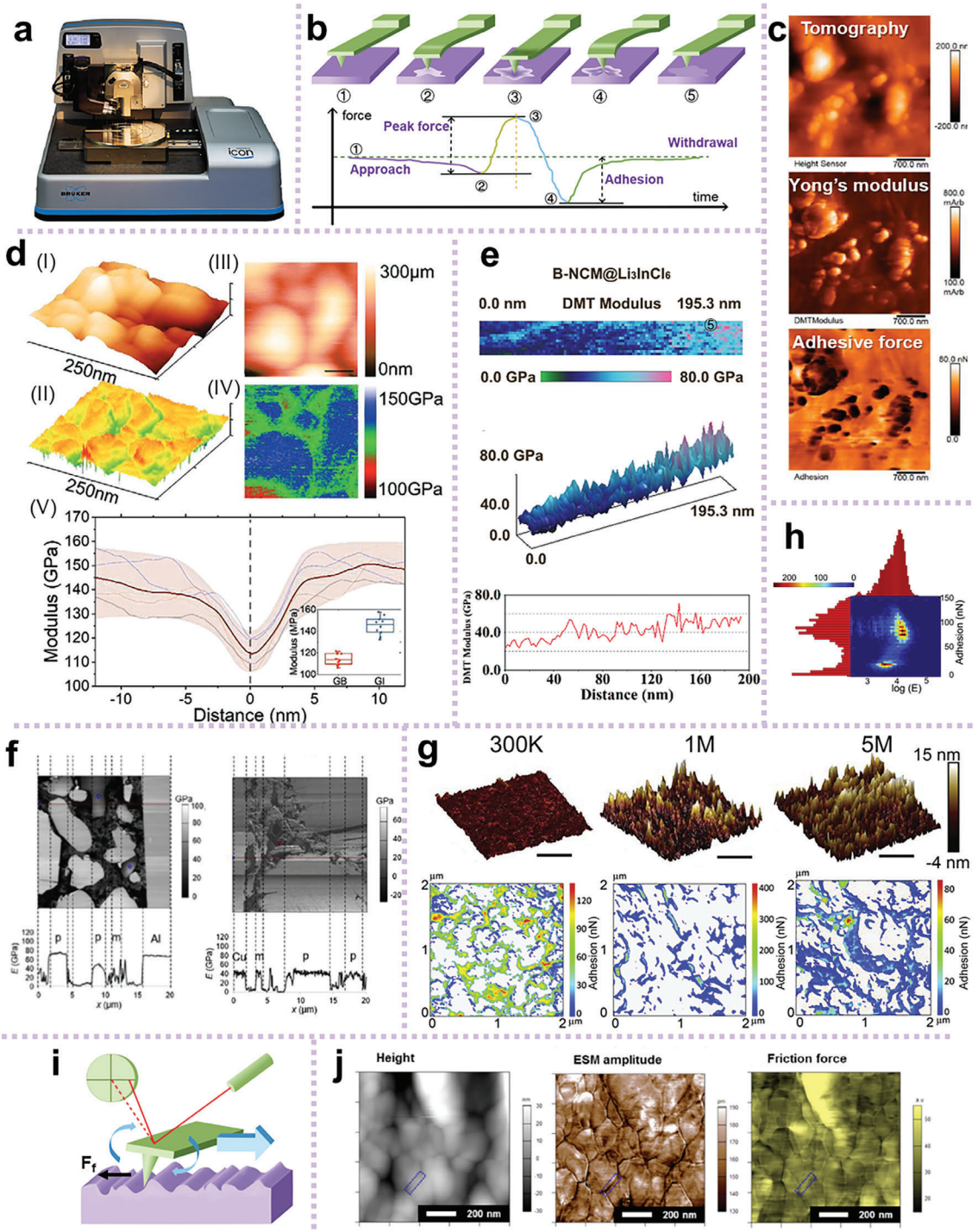


Figure 6. Collection of mechanical tests on AFM. a) Photo of AFM equipment b) Schematic of the adhesion test principle and force curves; c) AFM tomography, Yong's modulus, and adhesive force images of LLZO-PEO($LiClO_4$) electrolyte at 55 °C. Adapted with permission[60] Copyright 2021, Elsevier; d) The morphology (d-I) and modulus mapping (d-II) of LLZO surfaces and corresponding 2D views (d-III-IV), (d-V) the relationship of modulus and distances to grain boundaries. Adapted with permission[61] Copyright 2021, Wiley-VCH; e) Young's modulus mapping (top), 3D images of the modulus (middle), and modulus curve (bottom) of NMC@Li_3InCl_6[62] Adapted with permission, Copyright 2023, RSC; f) Tomography and Young's modulus curves of the $LiCoO_2$ (left) and graphite (right) electrode cross-sections at 100% state-of-charge state. Adapted with permission[63] Copyright 2019, Elsevier; g) 3D topography images and corresponding adhesion maps of LLZO/PEO/$LiClO_4$ composite electrolytes with different PEO molecular weight. Reproduced with permission[64] Copyright 2020, Cell Press h) Adhesion and Young's modulus histogram of LLZO/PEO/$LiClO_4$ composite electrolytes. Reproduced with permission[64] Copyright 2020, Cell Press; i) Schematic of the friction test principle; j) Morphology, ESM amplitude, and friction force images of solid electrolyte (lithium silicon titanium phosphate) composited with graphite anode. Reproduced with permission[65] Copyright 2020, Wiley-VCH.

© 2024 The Author(s). Advanced Energy Materials published by Wiley-VCH GmbH

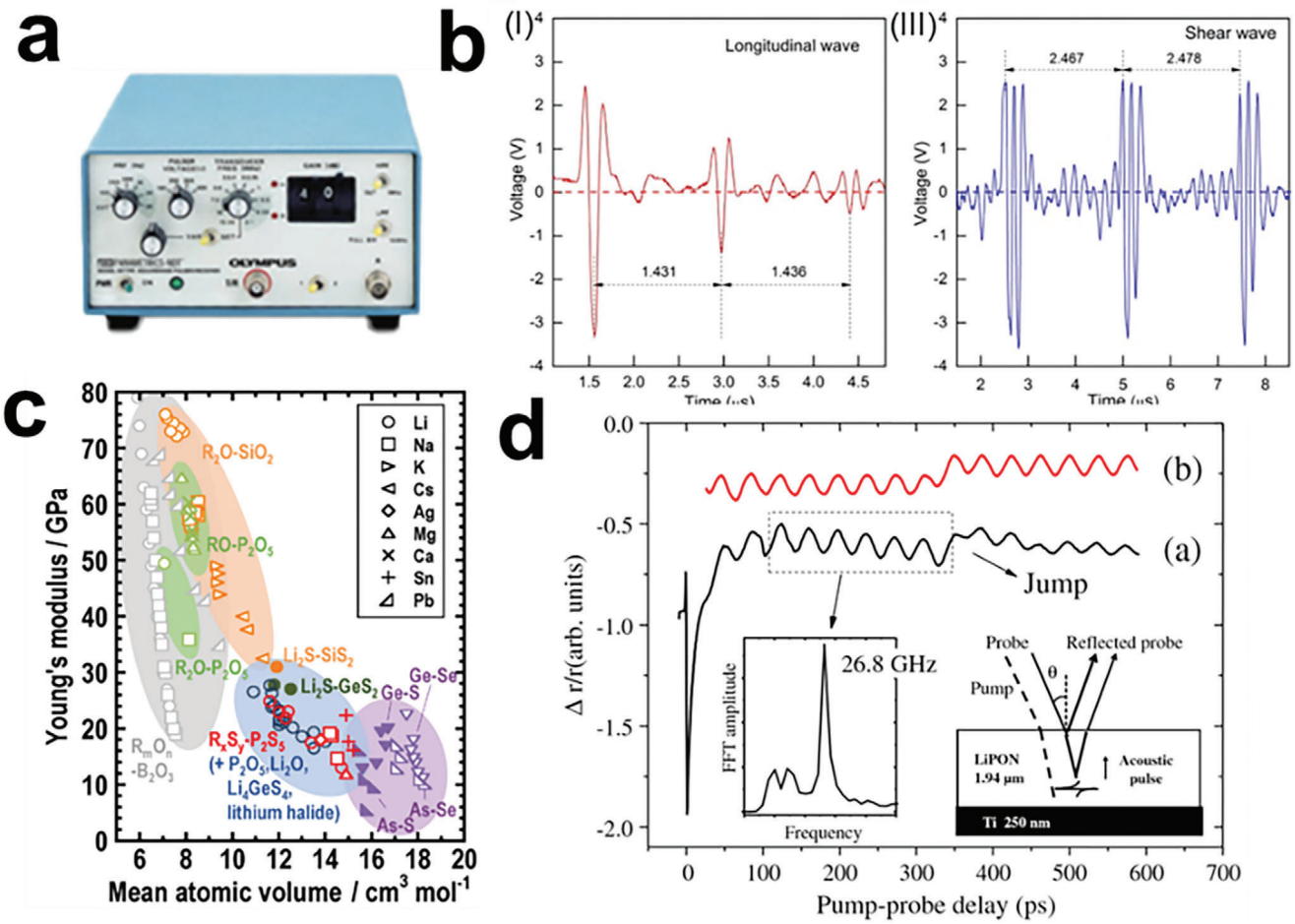


Figure 7. Collection of mechanical tests on ultrasonic sound velocity technique. a) Photo of a square wave pulser-receiver used in the ultrasonic pulse-echo technique; b) Representative pulse-echo spectra of bulk NCM in (I) longitudinal and (II) shear waves; Adapted with permission[66] Copyright 2017, Elsevier. c) The relationship between mean atomic volumes and Young's modulus for different electrolyte systems; Reproduced according to the terms of the CC-BY license[67] Copyright 2018, published by the Ceramic Society of Japan. d) the transient reflectivity signal measured by picosecond ultrasonics technique. Reproduced with permission[76] Copyright 2013, Elsevier.

More meticulous characterization is needed to reflect complex interactions, which currently remain insufficient.

3.2. Compression Modulus (E_C)

Definition: The compression modulus (E_C) describes the resistance of samples to external compression force, defined as $E_C = \sigma/\varepsilon$ where σ and ε represent the compression stress and corresponding strains, respectively. A higher compression modulus means the compressibility is lower. It is reflected in the maximum slope of the compressive stress-strain curves. If the compression force is uniaxial, the modulus also belongs to Young's modulus. In this case, the compression modulus is regarded as approximately equal to the tensile modulus, because both of them reflect the barriers forcing atoms to deviate away from equilibrium positions in two adjacent atoms. If the force is in three axes, it corresponds to the bulk modulus.

Universal Testing Machine: Similar to the tensile modulus, the compression modulus can also be calculated from stress-strain curves obtained from a universal testing machine. Material can be cast into a cylindrical shape (Figure 4d(ii)) for compression tests, in contrast to the "dog-bone" shape (Figure 4d(i)) for tensile tests, as shown in the investigations by William et al.[50] In their work, an epoxy resin-based plasticized polymer electrolyte was developed. By simultaneously increasing the contents of LiTFSI (from 1.5 wt% to 30 wt%) and through the addition of propylene carbonate (as a plasticizer, from 5.0 wt% to 15.9 wt%), the compression modulus and ultimate compressive strength were found to decrease from 10.45 to 6.95 Mpa and ultimate compressive strength from 2.55 to 1.23 Mpa. Ziyang et al.[44] designed a crystallohydrate-polymer composite electrolyte for solid-state supercapacitors (Figure 4e). The intermediate water layers between hydrated salts and polymer chains contributed to high compression strength. In changing the precursors' ratio between sodium thiosulfate pentahydrate and sodium polyacrylate from 2 to 10, the compression modulus of composite electrolytes was dramatically improved from 4.941 to 197.773 Mpa. Mingming et al.,[45] compressed a reduced graphene oxide (rGO) hydrogel filled with phosphoric acid/polyvinyl alcohol (H_3PO_4/PVA), a nearly linear

© 2024 The Author(s). Advanced Energy Materials published by Wiley-VCH GmbH

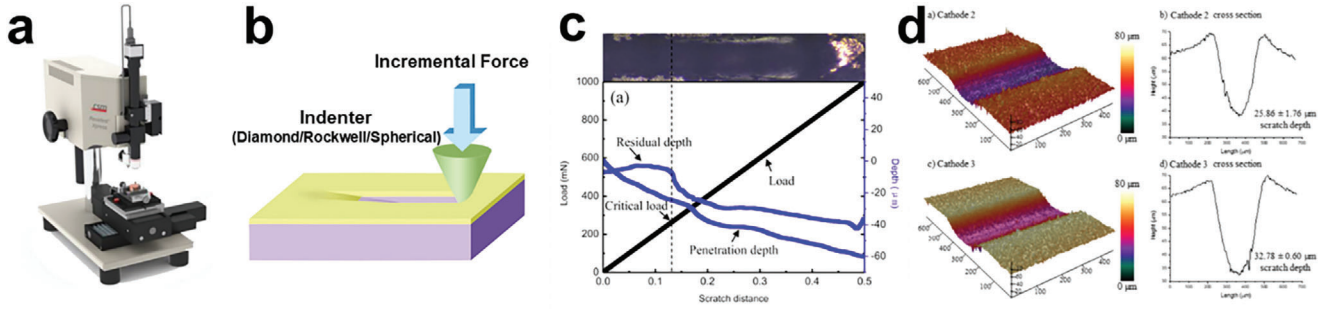


Figure 8. Scratch testing on solid-state batteries. a,b) Photo (a) and schematic (b) of the nanoscratch tester; c) Typical profiles of the penetration depth and residual depth after nanoscratch test on PVDF-based Co_3O_4 electrodes. Reproduced with permission[95] Copyright 2015, Elsevier; d) 3D optical microscope images of the scratches on commercial cathodes. Reprocued with permission[96] Copyright 2020, ACS.

region of elastic portion and a plateau stage was observed due to the yield in densified graphene architectures, as shown in their stress–strain curves (Figure 4f).

Nanoindentation: The nanoindentation technique can also be used to evaluate the elastic modulus of a material. The nano-indenter instrument and schematic diagram are shown in Figure 5a,b. In forcing the indenter tip into the sample surface, both elastic and plastic deformation can happen, but only the elastic deformation can be recovered. Therefore, the elastic modulus can be extracted from the unloading curve. There

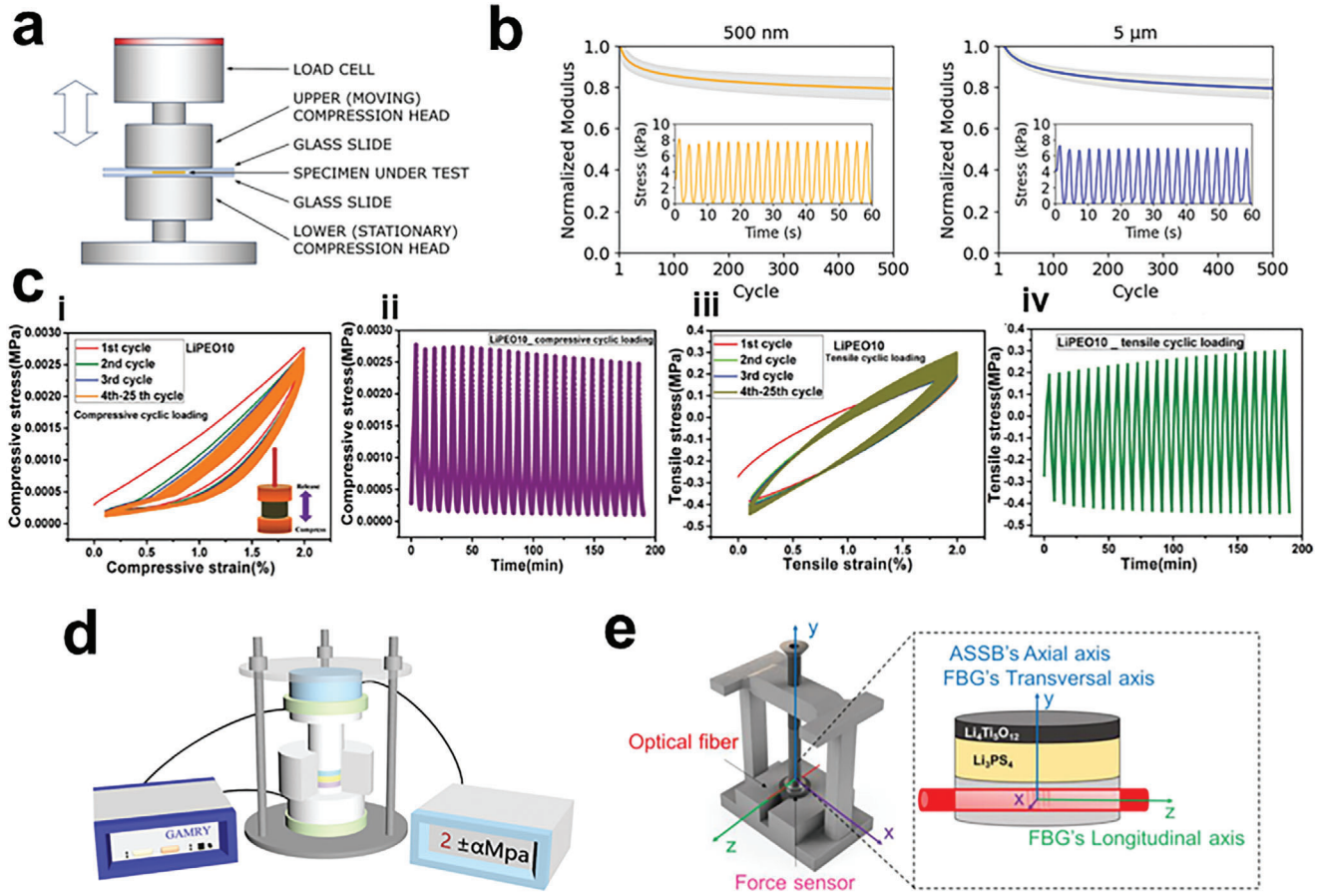


Figure 9. Mechanical fatigue testing on solid-state batteries. a) Schematic of mechanical compression test on a fatigue testing machine. Reproduced with permission[107] Copyright 2023, ACS and b) normalized modulus versus cycle numbers for PEO-LiTFSI electrolytes with different LLZTO sizes. Reproduced with permission[107] Copyright 2023, ACS; c) Hysteresis curves (i, iii) and corresponding stress-time curves (ii, iv) of the PEO/$LiClO_4$ polymer electrolytes under the compression mode (i, ii) and tensile mode (iii, iv). Adapted with permission[108] Copyright 2019, Wiley-VCH; d,e) Schematic of bespoke devices: the external pressure sensor added on a specific battery case (d), and the built-in optical fiber Bragg grating sensor added on the modified coin cell (e). Reproduced with permission[109] Copyright 2022, Springer Nature.

© 2024 The Author(s). Advanced Energy Materials published by Wiley-VCH GmbH

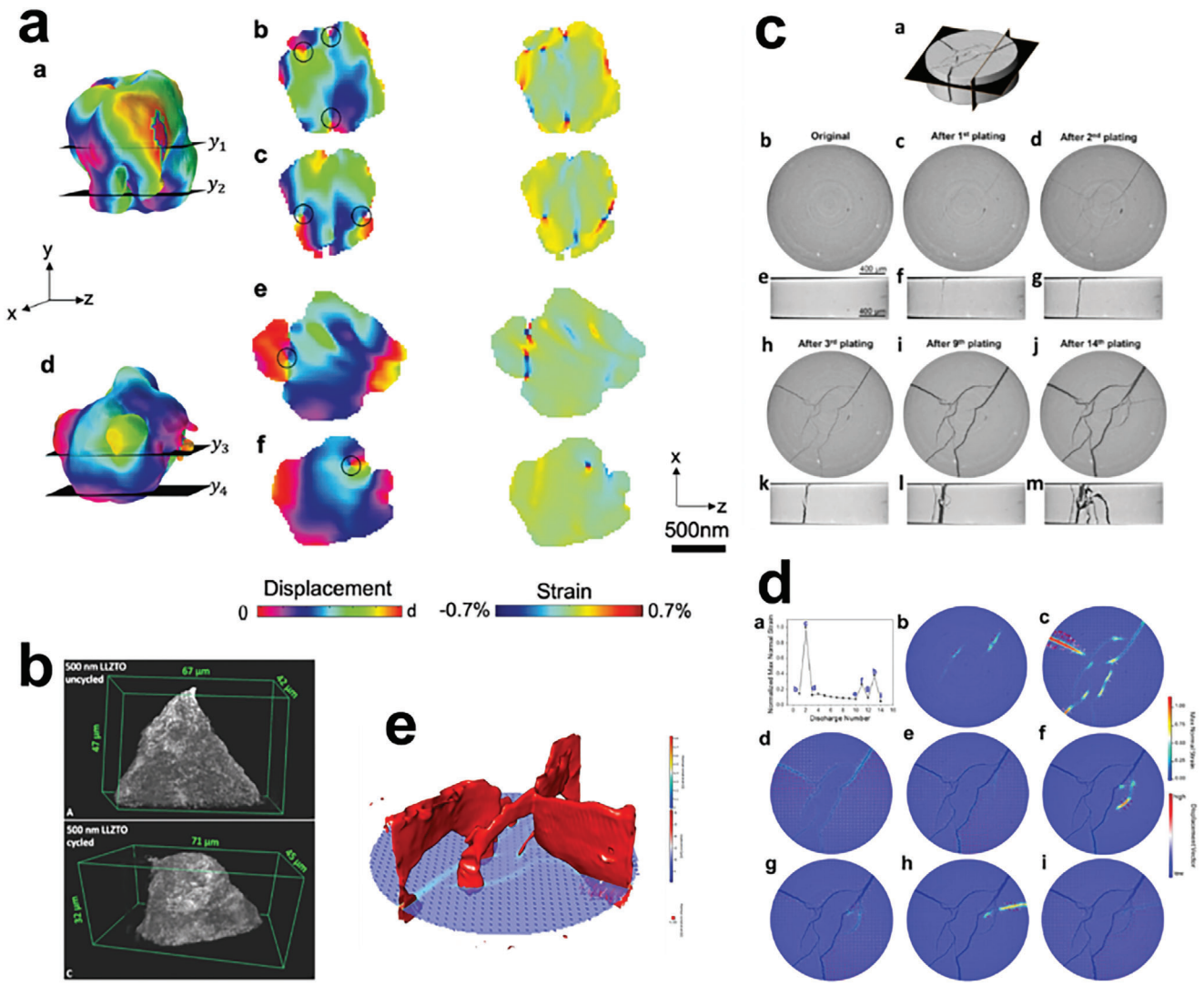


Figure 10. X-ray facilities on mechanical testing solid-state batteries. a) The reconstructed 3D displacement field of LLZO grains with the (a) mixed and (d) cubic structure, and the xz cross-section of the displacement (middle) and the calculated strain maps (right). Reproduced with permission[114] Copyright 2021, ACS; b) 3D X-ray tomography of PEO-LiTFSI electrolytes before (up) and after (bottom) 500 cycles of mechanical compression. Reproduced with permission[107] Copyright 2023, Wiley-VCH; c–e) 3D tomogram and orthogonal slices during lithium plating (c) and corresponding strains (d), and 3D iso-surface configuration after the 2nd plating (e). Reproduced with permission[19] Copyright 2021, Elsevier.

are several kinds of indenter tips with different shapes, including the cone, crop, sphere, and wedge. They also have elastic deformation, so the corresponding modulus calculated from load-displacement curves is named the reduced elastic modulus. Kingsley et al.[46] tested a polymer electrolyte of polyvinyl alcohol (PVA) / polyvinylpyrrolidone (PVP) with $LiClO_4$ salt. A Berkovich indenter tip in a wedge shape was used because its large included angle increases the contact area with samples. Figure 5d shows the 3D images of this polymer electrolyte after loading at 5000 μN. The reduced modulus was changed in different $LiClO_4$ contents from 1 to 5 wt%, as shown in the load-displacement curves (Figure 5c) where a maximum reached 6.87 GPa. Gang et al.[51] tested an LLZO pellet with a loading of 400 mN and an indenter penetration depth of ≈3 μm. The elastic modulus was 106 GPa, representative of the material in its dense state demonstrating that controlling the mixture can optimize robust films. Zhezhen et al.[52] compared the thin LLZO sample by tape casting with the bulk LLZO pellet by die pressing, and found the elastic modulus of the thin electrolyte was ≈155 GPa, higher than 142 GPa of the bulk samples. Therefore, by this measure, thin LLZO samples have higher resistance to the growth of lithium dendrites.

If the nano-indenter instrument is combined with other characterization equipment, comprehensive information can be obtained. Jack et al.[53] mounted a nano-indenter onto the sample stage of an SEM which was also equipped with electron backscattered diffraction (EBSD), as shown in the schematic in Figure 5e(iii). Lithium metal was characterized by EBSD before and after nanoindentation tests so that the dependence of mechanical properties on crystallographic orientation can be revealed. As shown in Figure 5e(iv), the indents along vectors near the <100> axis of the crystal have lower indentation modulus

© 2024 The Author(s). Advanced Energy Materials published by Wiley-VCH GmbH

(11 GPa) than those near the <111> direction (14 GPa), indicating the lithium is highly anisotropic in elasticity. Hugues–Yanis et al.[54] polished the $LiMn_2O_4$ cathode in cycled batteries, and cut it further by FIB. Then, it was possible to do nanoindentation tests selectively on any $LiMn_2O_4$ particles or the adjacent matrix, as shown in Figure 5f. Although this sample was from a liquid electrolyte system, the method can be utilized to analyze the composite cathode in solid-state batteries.

Atomic Force Microscope (AFM): Atomic Force Microscope (Figure 6a) which is widely utilized to characterize surface morphology, can also measure Young's modulus as well as adhesive force (detailed discussion in Section 3.6.1). Using Peak Force quantitative nanoscale mechanical (QNM) mode, the AFM tip approaches the sample first, until it contacts the sample surface and reaches a peak force. Then, the tip will be moved away from the sample surface by a reversed force. The processes of adhesion will be reflected on the force curves, as schematically illustrated in Figure 6b. The adhesive forces are obtained from the curves, and Young's modulus at this point can be calculated based on the Derjaguin–Muller–Toropov model. Therefore, the distribution of Yong's modulus and adhesive force, together with surface morphology, can be captured in the same area simultaneously. Significantly, the resolution is at the nanometer scale, much higher than in the two measurement methods mentioned above.

Based on this method, Cai et al.[60] obtained Young's modulus distributions as well as the adhesive force and surface morphology in LLZO/PEO ($LiClO_4$) composite electrolytes, shown in Figure 6c. With the temperature increasing from 30 to 60 °C, Young's modulus decreased obviously as the PEO chains transformed into a first amorphous then viscous fluid state. Ziheng et al.[61] mapped the modulus on LLZO surfaces and compared it with their morphology, as shown in Figure 6d. On average, the modulus of LLZO decreased from ≈145 GPa in grain interiors to ≈120 GPa at grain boundaries. This mechanical inhomogeneity could assist the crack extension and lithium deposition along grain boundaries. Zichen et al.[62] evaluated the Yong's modulus of NMC@Li_3InCl_6 composite cathodes prepared by different processing routes. Figure 6e shows Yong's modulus mapping, 3D images of the modulus, and corresponding modulus curves. It was found a ball milling treatment remarkably improved the mean Yong's modulus to 35.3 GPa, an order of magnitude higher than that (2.31, 2.28 GPa) of samples prepared by other milling conditions and procedures. Besides, Young's modulus of SEI layers in Li/K metal anodes can be measured with this method as well.[9]

Furthermore, the AFM with a bimodal amplitude modulation mode combines the simplicity of amplitude-modulated (AM) operation with the high sensitivity and signal-to-noise ratio of frequency-modulated (FM) operation. This AM-FM imaging mode allows for measuring a large range of moduli (0.1–100 GPa) at a very fast scan speed. With this method, Hiroki et al.[63] quantitatively analyzed Young's modulus on cross-sections from $LiCoO_2$-based cathode and graphite-based anode in an electrodes' range. As shown in Figure 6f, a few cathode particles were observed to have significantly smaller Young's modulus at 100% state-of-charge state, which could be caused by incomplete or over-delithiation. The characterization method can be cross-referenced to investigations on solid-state batteries, although it was conducted on liquid electrolyte cells in this research.

In addition to measuring the compression modulus directly, many specialized battery cases are equipped with pressure sensors. So that the compression pressure inside cells is monitored all the time. This will be discussed in Section 3.8.

3.3. Shear Modulus (G)

Definition: The shear modulus evaluates the ability of a material to resist transverse deformation under shear stresses. It is defined as a ratio of shear stress to the corresponding strain ($G = \tau/\gamma$, τ, and γ represent the shear stress and shear strain, respectively). The ratio of transverse strains to axial strains is defined as Poisson's ratio (υ). Normally, the shear modulus is widely used to characterize metals in engineering.

Measurement and Application Examples in SSB: Traditionally, the shear modulus is tested by a shear strength testing machine, however, it is generally more convenient to use the ultrasonic sound velocity technique to measure the solid electrolyte or electrolyte materials in solid-state batteries. This nondestructive technique acquires the longitudinal velocity (v_L) and shear velocity (v_S) of ultrasonic sound that passes through the samples. If the density (ρ) of the material is known, the shear modulus is calculated from the formula: $G = \rho \bullet v_S^2$. Meanwhile, the elastic modulus (E) and Poisson's ratio follow the equations: $E = \rho \bullet v_S^2 \bullet (3v_L^2 - 4v_S^2)/(v_L^2 - v_S^2)$; $\upsilon = (v_L^2 - 2v_S^2)/[2(v_L^2 - v_S^2)]$. Figure 7a shows one of the most widely used tests apparatus-the ultrasonic pulser-receiver. Eric et al.[66] obtained representative pulse-echo spectra of bulk NCM, as shown in Figure 7b. The time gap between subsequent echoes for the longitudinal and shear waves was directly obtained from the spectra. Then, the corresponding velocities were found to be 7152.0 and 4147.2 m s^{-1}, respectively. The shear modulus, elastic modulus, and Poisson's ratio were calculated to be ca. 77.9, 194.3 GPa, and 0.25, respectively. With this method, Atsutaka et al.[67] measured the solid electrolyte of the Li_2S-P_2S_5 system, finding an increasing Young's modulus (i.e., elastic modulus) with changes to the composition. The correlations between Young's modulus and a defined mean atomic volume are provided in Figure 7c, in comparison with three other material systems: oxide[68–70] and sulfide[71–75] solid electrolytes were characterized to establish the influences of chemical component and synthesis conditions on the shear and elastic modulus. In addition, the ultra-short acoustic wave, that is the picosecond ultrasonic wave, has the same function. Xu et al.[76] employed the picosecond ultrasonic method to detect the elastic properties of lithium phosphorous oxynitride (LiPON) thin films, as shown in Figure 7d. An acoustic wave was generated from the Ti layer and traveled into the LiPON film. Although the thickness of LiPON film was only 1.94 μm, it can be measured precisely in this way.

The ultrasonic technique is also suitable for detecting composites as well as layered structures. Therefore, it shows unique advantages for the investigation of composite cathode in solid-state batteries. The shear behavior in solid-state batteries has been largely overlooked and its properties are rarely reported. Considering the different operating conditions of solid-state batteries in practical, the shear and other deformations call for more attention.

© 2024 The Author(s). Advanced Energy Materials published by Wiley-VCH GmbH

3.4. Hardness (H)

Definition: Hardness reflects the resistance to localized plastic deformation induced by indentation or abrasion. It is dependent on several properties of materials, such as ductility, plasticity, strength, viscoelasticity, etc. Based on the different external forces, it can be divided into three types: indentation hardness, scratch hardness, and rebound hardness. There are different calculation formulas and units of hardness in different testing methods, as discussed in following.

Measurement and Application Examples in SSB: The indentation hardness is obtained by measuring the critical dimensions (diameter, depth, diagonal) of an indentation resulting from a specifically shaped indenter. Different indenter shapes, including the ball, cone and pyramid, correspond to different types of hardness, such as the Brinell hardness, Rockwell hardness or Vickers hardness. The scratch hardness tests the scratch width after forcing a rigid tip into the sample surface by using a Turner-sclerometer, which is also named Mohs hardness. The rebound hardness measures the "bouncing" height of a diamond-tipped hammer after dropping it onto the sample, by using a scleroscope. These measurements above describe the macroscopic properties with indentation or scratching marks in millimeters. Asma et al.[77] used Vickers indentation to correlate the hardness of LLZO with its grain size. They observed that the hardness decreased from 9.88±0.49 to 6.86±0.49 GPa when the grain size was increased from 5 to 600 μm. The relationship was given as $H = 6.80+6.93d^{-1/2}$, where d represents the grain size.

Besides the traditional testing methods mentioned above, the hardness can also be tested on a nanoscale by utilizing a nanoindenter which is more widely applied in solid-state battery research. From the load-displacement curves the contact stiffness, contact depth and contact area can be obtained. Then, the hardness is calculated from $H = P_{max}/A$, where P represents the maximum load and A represents the contact area. Importantly, almost all kinds of solid electrolytes (ceramic,[52,56,78–81] polymer,[46,82] composite)[83–85] are able to be measured by this method. Marc et al.[56] systematically investigated the hardness of both sulfide (LSPS, LPSCl) and oxide (LAGP, LLZTO) electrolytes. Under the same load of 2000 μN, the smaller indentation displacement of oxide electrolytes demonstrated a higher hardness, in comparison with that of sulfide electrolytes (Figure 5g). They also found all these solid electrolytes experienced softening and higher compliance as the temperature grew, which was represented by a decreasing hardness. Lifa et al.[82] investigated the hardness of PEO-LiTFSI electrolytes with or without 10 wt% LLZO additives in varying pre-strain levels. The pre-strain made the hardness decrease in the thickness direction of the electrolyte film, although the in-plane tensile strength was significantly enhanced. Guozhen et al.[81] used the nanoindentation method to get the hardness of LiPON thin film and obtained the highest value of 5.8 GPa in different synthesis conditions. The hardness had the same trend as the elastic modulus in that case. The intrinsic hardness of cathode materials is hard to characterize in the native state of the battery electrode, therefore, Eric et al.[66] pressed the NCM power into a pellet with a diameter of 12.7 mm and a thickness of 4.0 mm. After polishing, the sample was nano-indented by a Berkovich tip and the hardness was found to vary in a range of 9.1–11.7 GPa in different grains. This provides the method for other powdered electrode materials.

Generally speaking, the hardness property is expected to influence both the interfacial contact and the dendrites and cracks inside electrolytes and electrodes. Getting the hardness of every component in solid-state batteries, especially the most common electrode and electrolyte materials, helps to analyze these interfacial properties. Moreover, establishing the hardness changes under different conditions has significance for understanding its performance and corresponding degradation. The limitation of traditional hardness tests and nano-indenters is that all of them are destructive at present.

3.5. Fracture Toughness (K_{IC})

Definition: Fracture usually causes the failure of materials or components. It includes two forms: brittle fracture and ductile fracture. The fracture toughness is evaluated by a critical stress intensity factor, K_{IC}, beyond which the cracks start propagating and fracture happens. It is determined by the formula $K_{IC} = Y\sigma\sqrt{c}$, where σ, c, and Y represent the applied stress, crack length, and sample geometry, respectively. When the intensity factor in materials is below the K_{IC}, the bulk material can ensure its integrity though there are cracks inside.

Indentation Method: To measure the fracture toughness, the indentation method is commonly used. By using the nanoindenter, cracks would form at the corners of the indentation. Different nano-indenter tips (like Vickers and Berkovich) correspond to different shapes of indentation marks (pyramid- and three-sided pyramid-shape), based on which the fracture toughness K_{IC} is calculated from different formulas. Varying cracks could be induced by the different types, such as half-penny crack and Palmqvist crack. As the formulas usually contain elastic modulus and hardness (e.g., For the Berkovich tip, $K_{IC} = \delta(E/H)^{1/2}Pc^{-3/2}$, in which δ, E, H, P and c represent the constant value, elastic modulus, hardness, indentation load and crack length, respectively), the fracture toughness is usually calculated after obtaining those parameters. Julian et al.[57] adopted this method to test the NASICON-type solid electrolyte with Al/Y substitution ($Na_{1+2x}Al_xY_xZr_{2-2x}(PO_4)_3$) for sodium batteries. As shown in Figure 5h, the cracks were observed after indentation, and their length was precisely measured and the fracture toughness was found to be 1.4±0.1 MPa $m^{1/2}$. Jeff et al.[9] first reported the fracture toughness of polycrystalline LLZO to be 0.86–1.63 MPa $m^{1/2}$. The fracture mode in LLZO was predominately trans-granular with both half-penny and Palmqvist typed cracks, revealed by FIB-SEM observation after indentation. More studies indicated that the load and critical current density of LLZO have little relationship with the fracture toughness (Figure 5i),[51,77] while the thin film can effectively improve the K_{IC}.[52] Similarly, the fracture toughness of Lithium lanthanum titanium oxide (LLTO) was measured to be 0.82–1.29 MPa $m^{1/2}$,[86,87] which decreased with the lithium content increasing. For testing the cathode materials, like NCM, LCO, LFP and so on, they need to be first pressed into pellet and get the elastic modulus and hardness by the nano-indenter. The fracture toughness could be calculated thereafter.[88–90] It was 0.72±0.07 MPa $m^{1/2}$ in the NCM in Xu et al.'s investigations.[88] This protocol could be extended to test

© 2024 The Author(s). Advanced Energy Materials published by Wiley-VCH GmbH

the composite cathode with larger amount of solid electrolyte in solid-state batteries.

Because the sulfide electrolytes are extremely sensitive to air, it is challenging to test their mechanical properties. Frank et al.[58] specifically designed an instrumented indentation device to immerse the sulfide electrolyte in mineral oil during the test (Figure 5j). The elastic modulus and hardness of amorphous Li_2S-P_2S_5 (70:30 mol%) electrolyte was obtained to be 18.5±0.9 GPa and 1.9±0.2 GPa, respectively. After measuring the crack length, the fracture toughness was found to be 0.23±0.04 MPa $m^{1/2}$. The mineral oil in this work was proven to be nonreactive with the sulfide, so can be employed extensively for other sulfide-based electrolytes.

Notched-Specimen Method: The notched-specimen method represents a group of test methodologies traditionally used for metallic materials or plastics. A straight notch is cut by diamond wafer blades in sample preparation. Then, under external forces in three/four-point bending or stretching on a universal testing machine, cracks will initiate from the notch and propagate as intended. There are different types of measurements that specify the notch shape, forces, sample size and corresponding calculation formulas. We will detail some of them in the following.

The single-edge notched beam method (Figure 4g) usually uses a U-shaped notch and is widely used for ceramic materials. Yali et al.[91] shaped the doped-LLZO into a bar with a dimension of 3 × 4 × 35 mm. The notch had a width of ≈0.25 mm and a depth of ≈2 mm. The fracture toughness was found to be 0.94 ± 0.055 MPa·$m^{1/2}$ by an average of five tests. Besides, the chevron-notched beam method with a V-shaped notch was able to test solid electrolytes in solid oxide fuel cells,[92] also providing translational methods for solid-state batteries.

The fracture toughness in polymer-based electrolytes can be measured by single-edge notched tension testing. Kingsley et al.[46] made a PVA/PVP/$LiClO_4$ electrolyte into a designed shape with a crack on one side, as schematically shown in Figure 4h. Because of its high flexibility, the specimen was stretched to induce the crack growth until a final fracture. Based on the force-displacement curves in Figure 4i, the fracture toughness was found to be enhanced with $LiClO_4$ content increasing. It had a maximum of 0.5649 MPa·$m^{1/2}$ at 4 wt% $LiClO_4$. From the optical images during the fracture in Figure 4j, the notch tip was found to become blunt before crack initiation and void formation, and then cracks coalesced to form big cracks.

Pre-Cracking Method: For testing fracture toughness in ceramics, the method deploying a single edge pre-cracked beam is considered to be accurate. First, an indentation is made at the sample surface, as illustrated in Figure 4k. Then, cracks are initiated by bridge pressure, and they propagate in a fixture with three-point bending until fracture. By this means, a glassy electrolyte of lithium borophosphate (LBP, the chemical formula is xLi_2O-(100-x)($0.5B_2O_3$-$0.5P_2O_5$)) was tested by Zhimin et al.[47] When the lithium content increased from 38mol% to 45mol%, the K_{IC} value was found to decrease from 0.76 to 0.56 MPa·$m^{1/2}$ (Figure 4l,m). This was governed by a bond switching of boron as it dissipated the strain energy during fracture.

In brief, fracture toughness is an important mechanical parameter in solid-state batteries, as it can predict the fast fracture of solid electrolytes and the abrupt failure of cells. It will be greatly valuable to develop characterization methods further, especially in improving the resolution, benefiting studies of the fracture mechanism and predictions of early-stage fracture.

3.6. Adhesive Force (F_{ad})

Definition: Adhesive Force describes the tendency of two surfaces or particles to cling to each other. There are different mechanisms in adhesion: specifically, chemical adhesion includes covalent bonding, ionic bonding, and hydrogen bonding that forms a compound at two separate surfaces. Mechanical adhesion happens when the adhesive materials fill into voids or pores on the surfaces of another material and interlock. Besides, the van der Waals force in dispersive materials, electrostatic force in conducting materials, and diffusive force in polymers can also function in adhesion.

In solid-state batteries, the adhesive force is very important as they strongly effect on the interfacial contact and delamination at various interfaces, especially the interfaces between solid electrolyte and electrode film. The contributing factors of adhesion include the physical properties of solid electrolyte, processes in cell assembly, cycling conditions and so on. Whilst they are utilized to evaluate and compare specific materials, the testing methods for adhesive forces do not yet have a standard protocol yet which should be further developed.

Atomic Force Microscope: AFM (photo in Figure 6a) is one of the most important methods for the measurement of adhesive forces, especially at the nanoscale. As described in Section 3.2.3, the adhesive force is measured in AFM-QNM mode, as illustrated in Figure 6b. Marm et al.[64] mapped the adhesive force and surface roughness on the surfaces of LLZO/PEO/$LiClO_4$ composite electrolytes with different PEO molecular weights. The low molecular weight of PEO had relatively lower surface roughness, meanwhile, the adhesive force was larger and in a heterogeneous distribution, as shown in Figure 6g. It was attributed to the higher crystallinity of polymers in the amorphous region of the electrolyte. Besides, a strong positive correlation between the adhesive force and Young's modulus is reflected in Figure 6h. Similarly in this composite electrolyte, Cai et al.[60] observed the adhesion increase when the temperature was increased from 30 to 60 °C. Besides, Marm et al.[93] compared the adhesive forces in Li_3PS_4 and Li_6PS_5Cl electrolytes and their composite with PEO by this AFM-QNM mode. A large adhesive force was observed in the Li_3PS_4 electrolyte with a median value of ≈94 nN, while, the other three electrolytes showed similar median adhesion at ≈20 nN. Shiyuan et al.[94] verified a highly adhesive composite solid electrolyte by this means, which was compared with the normal PEO/LiTFSI electrolyte.

Scratch Test: Scratch testing evaluates the adhesion between a surface film and a substrate. A tip with great hardness scratches the sample surface; when the load is high enough to remove the surface film off of the substrate, it represents the adhesive force there. The scratch depth also reflects the adhesion ability. There are different kinds of scratch testers in microscale or nanoscale which have different tip dimensions and loading ranges. A nanoscratch tester is shown in Figure 8a,b. which was used by Jingjing et al.[95] who found the polyvinylidene difluoride (PVDF)-based Co_3O_4 electrodes had a remarkably improved adhesion with the Cu substrate after heating at 200 °C., wherein the critical load

© 2024 The Author(s). Advanced Energy Materials published by Wiley-VCH GmbH

was 266 mN (Figure 8c). Terreblanche et al.[96] scratched three kinds of commercialized cathode electrodes: after imaging by the optical profiler, the 3D morphologies of scratches were obtained on the cathode surfaces (Figure 8d). The cross-sectional plots of scratches showed a larger scratch depth in an aged cell, which was linked to the agglomerates of conductive carbon and binder. Similarly, the anode can also be measured by the balanced beam adhesion tester with a larger tip.[97]

Furthermore, the nano-indenter equipped with scanning probe microscopy can also be applied for the scratch test. With this method, Sashini et al.[59] obtained the 3D images of the nano-scratch imprint on the Si electrode composited with different binders, as shown in Figure 5k. The different adhesion was reflected in the depth and width of the scratch imprints. Also, the friction coefficient was quantitively calculated based on this scratch test.

The investigations mentioned above are in lithium batteries with liquid electrolytes, and these methods are recommended to be extended to measure the interfacial adhesion in various interfaces in solid-state batteries.

Peel Test: A peel test (also known vernacularly as a scotch-tape pull test or pull-off test), is used to evaluate the durability of protective coatings, such as paints, polymer coatings, metal coatings, etc. The adhesive force reflects the peeling strength between those two layers. In this test, as one end of layers is clamped, a layer is peeled off from the other at a fixed angle, also conducted on a universal testing machine. The adhesion is reflected in the peeling forces and the condition of layers and substrates. As shown in Figure 4n, Zhe et al.[48] peeled a modified Sn-bonded Si anode from Cu current collectors, after a tape was stuck to the electrode surface. The peeling force was found to be higher (9.0 N) compared to that (2.5 N) in the pristine Si, indicating an enhanced adhesive force in the Sn-bonded Si anode. Similarly, the adhesion ability of different binders in Si anodes can also be tested.[98] This method has great potential in characterizing solid-state batteries. Besides, following similar testing principles and conditions, this peel test can be conducted on a rheometer or peeling test machine. Xuewei et al.[49] used a rheometer to do 180-degree peeling tests and standard lap-shear tests on a PEO-based polymer electrolyte itself, as shown in Figure 4o. Resulting of the adhesion effect, the interfacial toughness and shear strength were 231.6±9.6. J m^{-2} and 71.3±8.1 kPa, respectively. Similarly, the adhesion between the electrolytes and electrodes, and between the electrolytes and current collectors, was systematically measured and compared. With a similar method, Hai et al.[99] investigated the influence of ionic liquid on adhesive strength, and Xueyan et al.[100] obtained the adhesion energy between a highly viscoelastic electrolyte and the LFP cathode/ electrolyte composite to be >160 J m^{-2}. Besides, Xin et al.[101] found the adhesion energy of PEO electrolyte to V_2O_{5-x} electrode decreased from 6.8 to 1.6 J m^{-2} after electrochemical cycling. Using peeling measurements enabled by a spring-loaded thrust meter, Wei et al.[102] evaluated the sticky interface between Li anode and sulfide-based electrolyte with a peel strength of 18.75 N m^{-1}. In a different way, Michael et al.[103] measured the adhesive strength of the Li-LLZO interface in a uniaxial tensile test. The Li anode was vertically separated from LLZO and this process was associated with the interfacial resistance.

To conclude, the adhesive forces act as one of the main forces to maintain intimate interfaces even during electrochemical induced volume changes. From the application examples summarized here, it can be seen that the characterization of adhesive force in solid-state batteries remains in its infancy. Many tests, like the scratch and peel tests, should be extended to application in solid-state batteries for measuring the polymer/composite electrolytes. The detachment trend of composite electrodes from current collectors is also valuable to be evaluated by this means.

3.7. Friction Force (F_f) and Friction Coefficient (μ)

Definition: Friction force (F_f) reflects the interfacial resistance in two contacting bulks when relative movement happens. In the macroscale, it follows the formula of $F_f = \mu N$, where N is the normal pressure and μ is the friction coefficient. While, in the microscale, it is directly proportional to the real contact area (A), following $F_f = \sigma A$ where σ is the shear stress. Usually, the bulk surfaces are quite uneven and rough at the microscopic level, and the resistance forces are generated along with heat production. As the movement in different layers of solid-state batteries is unavoidable during volume changes, it is well worth considering the friction, which remains seldom studied to date.

Measurement and Application Examples in SSB: Friction force determination at the microscale is not easy: one type of AFM named lateral force microscopy (LFM) can detect friction in a contact mode. As schematically shown in Figure 6i, LFM monitors the torsion of the cantilever in lateral directions (different from its deformation in vertical directions caused by the morphological changes in height), which results from the friction force acting on the cantilever in scanning across the sample surfaces. The magnitude of this torsion is measured and proportional to the friction coefficient.

The distribution of friction force on a composite of lithium silicon titanium phosphate (solid electrolyte) and natural graphite (anode materials) was obtained in Hongjun et al.'s work.[65] As shown in Figure 6j (right image), the grain shape was resolved with valleys in brighter contrast compared to the adjoining grains. Importantly, there is a very bright region observed at the top of the image which corresponds to the "sticky" binder of styrene-butadiene rubber and carboxymethyl cellulose in the composite. This was hardly distinguished in the normal morphological image by AFM or the amplitude image of electrochemical strain microscopy (ESM), as compared in Figure 6j. Therefore, the friction force measurement can function as a new method to differentiate phases in similar morphologies. In a similar manner, Xianke et al.[104] imaged the friction distribution on a composite electrolyte of PEO/PAA/MWNT (PAA: poly (acrylic) acid, MWNT: multi-walled carbon nanotubes). The MWNT and PEO/PAA were distinguished clearly because the MWNT has a lower friction coefficient than that of PEO and PAA. Moreover, Quang et al.[105] studied the different friction forces on a Si anode with various polymer binders, and compared them before and after immersing into liquid electrolytes. They found that the nanoscale friction against Si significantly decreased because of immersion into the liquid electrolytes, while, the friction fluctuation increased due to an increase in surface asperities. Hua et al.[106] observed a "stick-slip" event in the friction trace, when

© 2024 The Author(s). Advanced Energy Materials published by Wiley-VCH GmbH

they tested the interfaces of a solvated ionic liquid and highly ordered pyrolytic graphite which was highly influenced by the potential on interfaces.

In brief, the friction distribution can be visualized by the LFM technique, which has unique advantages in distinguishing different components in composites and acquiring their morphology information simultaneously. If coupled with other techniques (like ESM), different phases can be characterized more comprehensively. In solid-state batteries, the friction forces among different layers are barely known, and greater understanding is needed to further elucidate the effect of this parameter which would be enabled by further developments in characterization methods.

3.8. Mechanical Fatigue

The mechanical fatigue describes the mechanical damage accumulated in materials during cycles of stress and strain. In the past, it has been widely used in testing structural materials and parts. Before the material is finally destroyed, three processes can happen in sequence, including crack initiation, propagation, and unstable fracture. In solid-state batteries, the asymmetric volume changes can cause cyclic compression and tensile forces inside the cells during charging and discharging which can break the solid electrolytes or other components. Therefore, mechanical fatigue is a critical issue, especially in practical applications. It is feasible to repeatedly compress or stretch the batteries or their components using fatigue testing machines or bespoke devices to simulate these mechanical processes.

By using a fatigue testing machine, the evolution of tensile or compression properties can be tracked during repeated mechanical processes. As shown in Figure 9a, Dan-il et al.[107] utilized the fatigue testing machine to compress the PEO/LiTFSI/LLZO composite electrolyte for 500 cycles with 30% strain. After cycling, the normalized modulus was found to reduce to ca. 80% of its original value, as shown in Figure 9b, and this fatigue softening was independent of LLZO particle size (in the range between 500 nm and 5 μm). This softening can lead to a weaker contact pressure at electrode/electrolyte interfaces, further deteriorating the electrical performance. Sudeshna et al.[108] conducted compression cycling tests and tensile cycling tests on PEO/$LiClO_4$ polymer electrolytes. Stress hysteresis was observed in the loading and unloading curves (Figure 9c). Interestingly, the cyclic compression softened the matrix, but cyclic tension can harden the matrix, and the ionic conductivities were affected in respective directions. This was because the anisotropic alignments of the polymers, that was induced by the processing history of the solid electrolyte, affected its mechanical responses. Besides, it is also possible to repeatedly stretch and compress the hydrogel polymer electrolytes.[110]

Bespoke devices are designed to measure the internal stress of batteries with a simultaneous recording of voltage curves. There are two types of devices: a specific battery case linking to an external pressure sensor (Figure 9d) and a modified coin cell with a built-in optical fiber Bragg grating sensor inside (Figure 9e). These devices are widely used in detecting sulfide electrolytes, which has previously been reviewed in the literature.[111–113] However, only pressure or stress can be tracked in these tests, leaving the evolution of other mechanical parameters unrevealed.

3.9. Crystal Internal Stress

As discussed in Section 2.5, internal stresses are already contained inside the crystalline material after synthesis and processing at the atomic scale. They can be measured by the Bragg coherent diffraction imaging (BCDI) at synchrotron facilities. By analyzing one or more crystal diffraction peaks, the lattice strain in a single nanoparticle can be obtained. With the help of this characterization, Yifei et al.[114] reconstructed the 3D field of atomic displacement inside LLZO grains with the cubic and tetragonal phases and calculated the corresponding strain, as shown in Figure 10a. The inhomogeneous strain field arose from the dislocations in both structures and existed at the unloaded state. They minimized the range of applied stresses that the LLZO grains can withstand without exceeding their ultimate strength.

3.10. The Strain Distribution

The strain distribution could visibly reflect the mechanical force conditions inside materials, which is very valuable in the failure analysis and prediction for solid-state batteries. X-ray computed tomography (CT) is able to provide the qualitative strain distribution in 3D: after acquiring the transmission projections at numerous angles, the 3D structure of the sample can be reconstructed and the strain can be calculated by a digital volume correlation method. Dan-il et al.[107] compared the 3D images of the PEO/LiTFSI/LLZO composite electrolyte before and after compression for 500 cycles (Figure 10b). The size distribution of LLZO particles, (500 nm or 5 μm in two samples), was found to be uniform and not significantly influenced by the compression cycling. Therefore, the microstructure was not the major cause of the softening behavior (introduced in Section 3.8). Shuai et al.[19] tracked the morphological revolution of Li_3PS_4 solid electrolytes during dendrite growth using in situ X-ray CT, and further extracted the corresponding strain distributions (Figure 10c,d). The steps of crack and dendrite propagation showed significantly larger stress and strain in the adjacent positions of LPS, which indicated the stresses arising in solid electrolytes worked as the driving forces for cracks.

Different from the measurements in Sections 3.1–3.7, the strains obtained in Sections 3.8–3.10 come from not only mechanical forces but also electrochemical and chemical forces, and the results reflect the coupled effects of different deformation origins, showing great potential in the comprehensive study of solid-state batteries.

3.11. Theory and Modeling

Theory and modeling are powerful methods to complement empirical investigations and to explore modes that are inaccessible by experiment. Density-functional-theory based first-principle calculations are widely used to investigate some mechanical parameters including solid electrolytes doped with various elements. Roland et al.[115] successfully obtained elastic modulus and hardness in Al^{3+}/Ta^{5+} doped LLZO with this method. Seungho et al.[116] compared the value of shear modulus of Ta^{5+} doped LLZO from measurement and calculation. Besides, the

© 2024 The Author(s). Advanced Energy Materials published by Wiley-VCH GmbH

stress–strain curves,[117,118] hardness,[119] fracture toughness,[47] and Poisson's ratio[120] of different solid electrolytes have been investigated as well. The basic mechanical parameters of common materials in solid-state batteries have been summarized in **Table 1**, with the calculated data labeled in italics and underlined.

Phase-field modeling with finite element analysis is extensively utilized to simulate some scenarios in SSB operation, such as dendrite growth and particle expansion, and it can also be coupled with electrochemical simulations. Shizhao et al.[121] systematically simulated the distributions of local stress fields under interfacial and internal defects with different shapes, sizes, and positions, together with their effects on crack propagation and corresponding damage. Jared et al.[122] visualized the fracture generated by interphase expansion, especially at the edges of a solid electrolyte. The driving forces of fracture were classified into radial stress and circumferential stress and their evolution and distribution were analyzed further. Besides, intentionally inducing the crack growth by external forces has been studied in combination with experiment and modelling in both Cole et al.'s[25] and Scott et al.'s[123] work. At the cathode, Robert et al.[124] compared the stresses occurring at the microscopic grain level by matching various cathode materials with different solid electrolytes, including PEO, LPS, LATP, and LLZO wherein the bulk moduli of electrolytes and the strain generated in the cathode governed the stress. Giovanna et al.[125] analyzed the influence of fracture energy of solid electrolyte and Young's modulus on cracks inside the composite cathode, which was linked to mechanical degradation. Additional studies of relevance can be found in the following references.[126,127]

4. Summary & Outlook

This review systematically introduces the mechanical parameters relevant to solid-state lithium batteries and discusses their corresponding characterization methods. As summarized in **Table 2**, many of the measurements follow testing methods previously used in other areas, whilst some have been specifically adapted or designed for solid-state batteries. Some characterization methods that are still not used in solid-state batteries but in related areas, are also cross-referenced to explore their translational possibilities in solid-state battery research.

Among the characterization methods in Table 2, the universal testing machine has advantages in multiple loading modes and simple sample preparation, whereas it reflects bulk properties at a large scale. In contrast, AFM and nanoindenter techniques provide measurement at the nanoscale, providing different testing modes for different parameters. However, they both require a relatively flat sample surface and the spring constant of the AFM tip also limits the testing range. Other methods, like the ultrasonic pulser-receiver, hardness tester and rheometer, test at the macro-scale, and therefore do not capture the detail of the changes in nanoscales. Bragg CDI shows unique abilities and is non-destructive, but the technique is only available at synchrotrons. The compatibility with in-situ/operando testing is also summarized in Table 2.

With deepening research on solid-state batteries, the comprehensive characterization methods on mechanical parameters are going to be utilized extensively and developed rapidly in the near future. In order to reveal the mechanical progress and mechanisms in solid-state batteries better, some future perspectives are outlined below.

i. More mechanical parameters should be considered and measured systematically in solid-state batteries. Besides the basic parameters measured in previous references (as summarized in Table 1), more mechanical parameters, such as torsional strength, impact strength, flexural strength, friction coefficient, etc., can evaluate the mechanical properties and processes, so that the mechanical issues in solid-state batteries can be revealed more comprehensively. The solid electrolyte and electrode materials need to be assessed and further improved in these properties to enhance the battery performance from the mechanical viewpoint. Meanwhile, the associated testing equipment should be applied in solid-state batteries with necessary modifications.
ii. Instruments need to be designed or modified to combine the mechanical measurements with other characterizations: It is necessary to detect the mechanical properties simultaneously with chemical, thermal, and electrochemical properties at the same region in solid-state batteries so that their relationship and interactions can be revealed. Therefore, the testing methodology should facilitate two or more kinds of characterization; for example, some successful work has been realized in combining the nano-indenter with the SEM, as shown in Figure 5e.[53] Besides, AFM-coupled SEM is an emerging technique that can directly observe the deformations forced by the AFM tip,[148,149] or even the electric conductivity.[148,150]
iii. In-situ/operando test techniques are needed for tracking more mechanical evolution processes during charging/discharging solid-state batteries. Though some mechanical processes have been tracked in situ (as discussed in Section 3.8), most of those successful in situ measurements have been limited to compression or tension. The evolution of other mechanical parameters in charging/discharging, such as hardness, fracture toughness, adhesive forces, etc., is seldom reported. Test equipment and methods have to be specifically designed and modified, and the temporal resolution of the mechanical characterization methods also needs to be raised greatly. With these improvements, it will become possible to reveal the dynamic changes in mechanical processes and their evolution during the cycling of solid-state batteries.
iv. Unified standards should be established to evaluate the mechanical properties of solid-state batteries. Some mechanical parameters used in engineering are measured by different instruments and calculated by different equations, resulting in different metrics. For example, as discussed in the hardness Section 3.4, this variously involves Vickers, Brinell, and Rockwell testers and the corresponding metric in each one. It is hard to compare their testing results directly and therefore limits standardization and comparison. Besides, as discussed in Section 3.6, there are different testing methods in adhesive force characterization, such as scratch test, peel test, and nano-indentation test. To solve this problem, unified standards on the measurement methods should be established so that different solid electrolytes, electrodes, and batteries can be compared from the mechanical perspective. This will have significant benefits for battery design and mass production in the long-term development of solid-state batteries.

© 2024 The Author(s). Advanced Energy Materials published by Wiley-VCH GmbH

Table 1. Summary of the mechanics parameters and corresponding testing methods, instrument, scale, testing objects, characteristics of tests, and related references (the items in italics and underline: not used in solid-state batteries).

Mechanics Parameter	Testing Methods	Instrument	Scale	Testing Object	Non-destructive	In-situ/ Operando	Coupled with Electrochemical tests	Refs.
Tensile modulus	Tensile test	Universal testing machine	micro	polymer/composite electrolyte; *composite cathode*			√	[30–40,127,129,130]
Compression modulus	Compression test	Universal testing machine	micro	polymer/composite electrolyte; *solid electrolyte for supercapacitor*			√	[45,50,44]
	Nanoindentation	Nanoindenter	nano	LLZO; polymer electrolyte; Li; *cathode*				[13–138]
		AFM (QNM & AM-FM mode)	nano	LLZO; composite electrolyte; cathode; SEI	√			[9,60–63]
Shear modulus	Ultrasonic sound	Ultrasonic puler-receiver	macro	LLZO; Li_2S-P_2S_5; LiPON; *Li; cathode*	√			[67–74,76,66,136]
Hardness	Indentation; scratch; rebound	Vickers/*Brinell/Rockwell hardness tester; Turner-sclerometer; scleroscope*	macro	LLZO; *cathode*				[68,77,134,137]
	Nanoindentation	Nanoindenter	nano	ceramic/polymer/composite electrolyte; *cathode*				[46,52,56,66,78–85, 131,132,139,140, 88–90,134–136,138]
Fracture toughness	Nanoindentation	Nanoindenter	nano	LLZO; LLTO; Li_2S-P_2S_5; *cathode*				[9,51,52,58,77,86, 87,141,88–90,135]
	Notched-beam method	Universal testing machine	micro	LLZO; polymer electrolyte				[46,91,142,143]
	Pre-cracking method			LBP				[47]
Adhesive force	Nanoindentation	AFM (QNM mode)	nano	composite/polymer electrolyte	√			[60,64,93,94]
	Scratch test	*Nanoscratch tester; Balanced beam scrape adhesion tester; Nanoindenter*	micro /nano	*binder; cathode/anode electrode*				[59,95–97,132]
	Peel test	rheometer; *Universal testing machine; peeling test machine*	micro	polymer electrolyte; *Si anode*				[49,99–103,48,98]
Friction force	Contact and scan	AFM (LFM)	nano	ceramic/composite electrolyte	√			[65,104,105,106]
Mechanical fatigue	Tensile/Compression cycling	Fatigue testing machine		polymer/composite electrolyte	√	√		[107,108,110]
		Home-made devices	micro /nano	sulfide electrolyte	√	√	√	[111]
Crystal internal stress	X-ray Diffraction	Bragg CDI	nano	LLZO	√	√		[114]
Strain distribution	Digital Volume Correlation	X-ray CT	micro & nano	ceramic/polymer/composite electrolyte	√	√	√	[107,115]

© 2024 The Author(s). Advanced Energy Materials published by Wiley-VCH GmbH

Table 2. Summary of the basic mechanical parameters measured in references (the items in italics and underlined: data from calculations).

Material	Young's Modulus, E [GPa]	Hardness, H [GPa]	Fracture Toughness, K_{IC} [MPa $m^{1/2}$]	Adhesive Force, F_{ad}[nN]
LLZO with doping	132.6–162.6[68,79]	5.2–9.1[68,79]	0.86–2.37[79,126]	–
Li_3PS_4	8.8–25;[71–73] *28.9–103.4*[128,129]	1.9±0.2[58]	0.23±0.04[58]	24[93]
LPSCl	*22.1–67.33*[129,130]	*4.958*[130]	–	22[93]
PEO	0.25–290.0MPa[131–134]	0.06–0.13[133,135]	0.41;[136] 232 (kJ m^{-3})[137]	10.4–20.7 (N)[134]
Li	3.0–21.2[138]	7–100 (MPa)[53,139]	–	–
NCM	179–201;[66,140] *14.98–265.90*[141]	7.78–14.29[66,140,142];	0.05-1.43;[88,142] 0.99–1.36 (composite)[143]	–
LCO	174–191[90,144]	8.2–11.7[90,144]	0.2–6.5[90]	–
LFP	182 (MPa) (composite)[145,146]	64–279.5 (MPa) (composite)[146,147]	–	–

v. Theoretical calculations and modeling should develop further along with the extension of research, especially in coupling with multiple physics and chemical processes. In building models, it is challenging but important to couple the mechano-chemo-thermal processes together, as the multiple physics fields can have interactions in between. Also, the accurate measurement of mechanical parameters is critical in assigning values. Besides, the simulations have advantages in capturing some transient state in changes. It should play a greater role in the study, as the time resolution of characterization would be limited in many cases. In combination with experimental characterizations and theoretical modeling, the investigations on mechanical processes in solid-state batteries will develop rapidly in the future.

Acknowledgements

The authors gratefully acknowledge the support of their research funders. P.R.S. acknowledges The Faraday Institution (FIRG061) and the Royal Academy of Engineering (CiET178/59). S.H. acknowledges the Fundamental Research Fund for the Central University, Nankai University (023/63243186) and the National Natural Science Foundation of China (22409099).

Conflict of Interest

The authors declare no conflict of interest.

Keywords

mechanical characterization, mechanical issues, mechanical parameters, solid-state batteries

Received: September 25, 2024
Revised: November 5, 2024
Published online:

[1] S. Kalnaus, N. J. Dudney, A. S. Westover, E. Herbert, S. Hackney, *Science* **2023**, *381*, 6664.
[2] Y. Koyama, T. E. Chin, U. Rhyner, R. K. Holman, S. R. Hall, Y. M. Chiang, *Adv. Funct. Mater.* **2006**, *16*, 492.
[3] W. P. Wang, J. Zhang, J. Chou, Y. X. Yin, Y. You, S. Xin, Y. G. Guo, *Adv. Energy Mater.* **2020**, *11*, 2000791.
[4] J. Choi, A. Manthiram, *J. Electrochem. Soc.* **2005**, *152*, A1714.
[5] L. de Biasi, A. O. Kondrakov, H. Geßwein, T. Brezesinski, P. Hartmann, J. Janek, *J. Phys. Chem. C* **2017**, *121*, 26163.
[6] R. Koerver, I. Aygün, T. Leichtweiß, C. Dietrich, W. Zhang, J. O. Binder, P. Hartmann, W. G. Zeier, J. Janek, *Chem. Mater.* **2017**, *29*, 5574.
[7] S. Deng, M. Jiang, A. Rao, X. Lin, K. Doyle-Davis, J. Liang, C. Yu, R. Li, S. Zhao, L. Zhang, H. Huang, J. Wang, C. V. Singh, X. Sun, *Adv. Funct. Mater.* **2022**, *32*, 2200767.
[8] M. V. Blanco, D. Devaux, A. M. Valtavirta, C. Cosculluela, Y. Watier, L. Quazuguel, M. Deschamps, M. Lecuyer, R. Bouchet, F. Cova, *J. Electrochem. Soc.* **2020**, *167*, 160517.
[9] D. Hwang, M. Y. Kim, Y. W. Song, L. HyoChan, S. J. Kim, B.-s. Kang, Y. Hong, H.-s. Kim, J. Kim, J. Lim, *Solid State Ionics* **2023**, *397*, 116245.
[10] Y. Qi, H. Guo, L. G. Hector, A. Timmons, *J. Electrochem. Soc.* **2010**, *157*, A558.
[11] T. Ohzuku, A. Ueda, N. Yamamoto, *J. Electrochem. Soc.* **1995**, *142*, 1431.
[12] L. Y. Beaulieu, K. W. Eberman, R. L. Turner, L. J. Krause, J. R. Dahn, *Electrochem. Solid-State Lett.* **2001**, *4*, A137.
[13] W. Zhang, D. Schröder, T. Arlt, I. Manke, R. Koerver, R. Pinedo, D. A. Weber, J. Sann, W. G. Zeier, J. Janek, *J. Mater. Chem. A* **2017**, *5*, 9929.
[14] W. Zhou, S. Upreti, M. S. Whittingham, *Electrochem. Commun.* **2011**, *13*, 158.
[15] C.-Z. Zhao, Y. Lu, J.-K. Hu, S. Sun, H. Yuan, Z.-H. Fu, X. Chen, J.-Q. Huang, M. Ouyang, Q. Zhang, *Sci. Adv.* **2022**, *8*, 0510.
[16] D. Cao, X. Sun, Q. Li, A. Natan, P. Xiang, H. Zhu, *Matter* **2020**, *3*, 57.
[17] L. Porz, T. Swamy, B. W. Sheldon, D. Rettenwander, T. Frömling, H. L. Thaman, S. Berendts, R. Uecker, W. C. Carter, Y. M. Chiang, *Adv. Energy Mater.* **2017**, *7*, 1701003.
[18] S. Hao, J. J. Bailey, F. Iacoviello, J. Bu, P. S. Grant, D. J. L. Brett, P. R. Shearing, *Adv. Funct. Mater.* **2020**, *31*, 2007564.
[19] S. Hao, S. R. Daemi, T. M. M. Heenan, W. Du, C. Tan, M. Storm, C. Rau, D. J. L. Brett, P. R. Shearing, *Nano Energy* **2021**, *82*, 105744.
[20] S. Kaboli, H. Demers, A. Paolella, A. Darwiche, M. Dontigny, D. Clement, A. Guerfi, M. L. Trudeau, J. B. Goodenough, K. Zaghib, *Nano Lett.* **2020**, *20*, 1607.
[21] M. Klinsmann, F. E. Hildebrand, M. Ganser, R. M. McMeeking, *J. Power Sources* **2019**, *442*, 227226.
[22] F. Zhang, Y. Guo, L. Zhang, P. Jia, X. Liu, P. Qiu, H. Zhang, J. Huang, *eTransportation* **2023**, *15*, 100220.
[23] J. M. Doux, H. Nguyen, D. H. S. Tan, A. Banerjee, X. Wang, E. A. Wu, C. Jo, H. Yang, Y. S. Meng, *Adv. Energy Mater.* **2019**, *10*, 1903253.
[24] Y. Qi, C. Ban, S. J. Harris, *Joule* **2020**, *4*, 2599.
[25] C. D. Fincher, C. E. Athanasiou, C. Gilgenbach, M. Wang, B. W. Sheldon, W. C. Carter, Y. M. Chiang, *Joule* **2022**, *6*, 2794.

© 2024 The Author(s). Advanced Energy Materials published by Wiley-VCH GmbH

[26] B. Liu, Y. Jia, C. Yuan, L. Wang, X. Gao, S. Yin, J. Xu, *Energy Storage Mater.* **2020**, *24*, 85.
[27] M. Naguib, S. Allu, S. Simunovic, J. Li, H. Wang, N. J. Dudney, *Joule* **2018**, *2*, 155.
[28] D. Xu, Y. Pan, X. Zhang, W. Dai, B. Liu, Q. Shuai, *Energy* **2024**, *290*, 130145.
[29] L. Yiding, W. Wenwei, L. Cheng, Z. Fenghao, *J. Cleaner Prod.* **2021**, *286*, 125451.
[30] L. Fan, *Solid State Ionics* **2003**, *164*, 81.
[31] Y. Li, Z. Sun, D. Liu, Y. Gao, Y. Wang, H. Bu, M. Li, Y. Zhang, G. Gao, S. Ding, *J. Mater. Chem. A* **2020**, *8*, 2021.
[32] W. Tang, S. Tang, C. Zhang, Q. Ma, Q. Xiang, Y. W. Yang, J. Luo, *Adv. Energy Mater.* **2018**, *8*, 1800866.
[33] X. Pan, Q. Hou, L. Liu, J. Zhang, M. An, P. Yang, *Ionics* **2021**, *27*, 2045.
[34] S. J. Park, A. R. Han, J. S. Shin, S. Kim, *Macromol. Res.* **2010**, *18*, 336.
[35] J. Ji, J. Keen, W. H. Zhong, *J. Power Sources* **2011**, *196*, 10163.
[36] Y. S. Ye, C. Y. Tseng, W. C. Shen, J. S. Wang, K. J. Chen, M. Y. Cheng, J. Rick, Y. J. Huang, F. C. Chang, B. J. Hwang, *J. Mater. Chem.* **2011**, *21*, 10448.
[37] M. Yuan, J. Erdman, C. Tang, H. Ardebili, *R. S. C. Adv.* **2014**, *4*, 59637.
[38] T. Sudiarti, D. Wahyuningrum, B. Bundjali, I. M. Arcana, *IOP Conf. Ser.: Mater. Sci. Eng.* **2017**, *223*, 012052.
[39] Q. Lu, J. Fang, J. Yang, G. Yan, S. Liu, J. Wang, *J. Membr. Sci.* **2013**, *425*, 105.
[40] Y. Li, Z. Sun, D. Liu, S. Lu, F. Li, G. Gao, M. Zhu, M. Li, Y. Zhang, H. Bu, Z. Jia, S. Ding, *Energy Environ. Mater.* **2020**, *4*, 434.
[41] X. Pan, F. Lian, Y. He, Y. f. Peng, X. m. Sun, Y. Wen, H. y. Guan, *J. Appl. Polym. Sci.* **2015**, *132*, 41839.
[42] H. K. Koduru, L. Bruno, Y. G. Marinov, G. B. Hadjichristov, N. Scaramuzza, *J. Solid State Electrochem.* **2019**, *23*, 2707.
[43] Y. Ji, K. Yang, M. Liu, S. Chen, X. Liu, B. Yang, Z. Wang, W. Huang, Z. Song, S. Xue, Y. Fu, L. Yang, T. S. Miller, F. Pan, *Adv. Funct. Mater.* **2021**, *31*, 2104830.
[44] Z. Tai, J. Wei, J. Zhou, Y. Liao, C. Wu, Y. Shang, B. Wang, Q. Wang, *Nat. Commun.* **2020**, *11*, 1843.
[45] M. Han, X. Wang, C. Chen, M. Zou, Z. Niu, Q. H. Yang, A. Cao, L. Song, J. Chen, S. Xie, *Energy Storage Mater.* **2018**, *13*, 119.
[46] K. Orisekeh, V. Anye, O. Oyewole, R. Ahmed, D. Orisekeh, O. Oyelade, S. Adeniji, S. Umar, A. Bello, W. Soboyejo, *J. Appl. Polym. Sci.* **2022**, *139*, e52379.
[47] Z. Chen, T. Du, S. S. Sørensen, R. Christensen, Q. Zhang, L. R. Jensen, O. V. Magdysyuk, M. Diaz-Lopez, M. Bauchy, Y. Yue, M. M. Smedskjaer, *J. Power Sources* **2023**, *553*, 232302.
[48] Z. Dong, W. Du, C. Yan, C. Zhang, G. Chen, J. Chen, W. Sun, Y. Jiang, Y. Liu, M. Gao, J. Gan, Y. Yang, H. Pan, *ACS Appl. Mater. Interfaces* **2021**, *13*, 45578.
[49] X. He, Z. Zhu, G. Wen, S. Lv, S. Yang, T. Hu, Z. Cao, Y. Ji, X. Fu, W. Yang, Y. Wang, *Adv. Mater.* **2023**, *36*, 2307599.
[50] W. T. Andrews, A. Liebig, J. Cook, P. Marsh, C. Ciocanel, G. E. Lindberg, C. C. Browder, *Solid State Ionics* **2018**, *326*, 150.
[51] G. Yan, J. F. Nonemacher, H. Zheng, M. Finsterbusch, J. Malzbender, M. Krüger, *J. Mater. Sci.* **2019**, *54*, 5671.
[52] Z. Fu, L. Zhang, J. E. Gritton, G. Godbey, T. Hamann, Y. Gong, D. McOwen, E. Wachsman, *ACS Appl. Mater. Interfaces* **2020**, *12*, 24693.
[53] J. Aspinall, D. E. J. Armstrong, M. Pasta, *Mater. Today Energy* **2022**, *30*, 101183.
[54] H. Y. Amanieu, D. Rosato, M. Sebastiani, F. Massimi, D. C. Lupascu, *Mater. Sci. Eng., A* **2014**, *593*, 92.
[55] L. Qian, H. Zhao, *Micromachines* **2018**, *9*, 654.
[56] M. Papakyriakou, M. Lu, Y. Liu, Z. Liu, H. Chen, M. T. McDowell, S. Xia, *J. Power Sources* **2021**, *516*, 230672.
[57] J. F. Nonemacher, S. Naqash, F. Tietz, J. Malzbender, *Ceram. Int.* **2019**, *45*, 21308.
[58] F. P. McGrogan, T. Swamy, S. R. Bishop, E. Eggleton, L. Porz, X. Chen, Y. M. Chiang, K. J. Van Vliet, *Adv. Energy Mater.* **2017**, *7*, 1602011.
[59] S. N. S. Hapuarachchi, K. C. Wasalathilake, J. Y. Nerkar, E. Jaatinen, A. P. O'Mullane, C. Yan, *ACS Sustainable Chem. Eng.* **2020**, *8*, 9857.
[60] C. Shen, Y. Huang, J. Yang, M. Chen, Z. Liu, *Energy Storage Mater.* **2021**, *39*, 271.
[61] Z. Lu, Z. Yang, C. Li, K. Wang, J. Han, P. Tong, G. Li, B. S. Vishnugopi, P. P. Mukherjee, C. Yang, W. Li, *Adv. Energy Mater.* **2021**, *11*, 2003811.
[62] W. J. Zichen Zhang, Y. Feng, R. Ai, J. Yu, X. Bie, X. Zhai, T. Jiang, S. Yao, F. Du, *Energy Environ. Sci.* **2023**, *16*, 4453.
[63] H. Sakai, Y. Taniguchi, K. Uosaki, T. Masuda, *J. Power Sources* **2019**, *413*, 29.
[64] M. B. Dixit, W. Zaman, N. Hortance, S. Vujic, B. Harkey, F. Shen, W. Y. Tsai, V. De Andrade, X. C. Chen, N. Balke, K. B. Hatzell, *Joule* **2020**, *4*, 207.
[65] H. Kim, J. Oh, G. Park, A. Jetybayeva, J. Kim, Y. G. Lee, S. Hong, *ACS Appl. Energy Mater.* **2020**, *3*, 3253.
[66] E. J. Cheng, K. Hong, N. J. Taylor, H. Choe, J. Wolfenstine, J. Sakamoto, *J. Eur. Ceram. Soc.* **2017**, *37*, 3213.
[67] A. Kato, M. Nose, M. Yamamoto, A. Sakuda, A. Hayashi, M. Tatsumisago, *J. Ceram. Soc. Jpn.* **2018**, *126*, 719.
[68] J. E. Ni, E. D. Case, J. S. Sakamoto, E. Rangasamy, J. B. Wolfenstine, *J. Mater. Sci.* **2012**, *47*, 7978.
[69] M. Tatsumisago, R. Takano, M. Nose, K. Nagao, A. Kato, A. Sakuda, K. Tadanaga, A. Hayashi, *J. Ceram. Soc. Jpn.* **2017**, *125*, 433.
[70] K. Nagao, M. Nose, A. Kato, A. Sakuda, A. Hayashi, M. Tatsumisago, *Solid State Ionics* **2017**, *308*, 68.
[71] A. Sakuda, A. Hayashi, Y. Takigawa, K. Higashi, M. Tatsumisago, *J. Ceram. Soc. Jpn.* **2013**, *121*, 946.
[72] A. Sakuda, A. Hayashi, M. Tatsumisago, *Sci. Rep.* **2013**, *3*, 2261.
[73] A. Kato, M. Yamamoto, A. Sakuda, A. Hayashi, M. Tatsumisago, *ACS Appl. Energy Mater.* **2018**, *1*, 1002.
[74] A. Kato, M. Nagao, A. Sakuda, A. Hayashi, M. Tatsumisago, *J. Ceram. Soc. Jpn.* **2014**, *122*, 552.
[75] L. L. Baranowski, C. M. Heveran, V. L. Ferguson, C. R. Stoldt, *ACS Appl. Mater. Interfaces* **2016**, *8*, 29573.
[76] F. Xu, L. Belliard, D. Fournier, E. Charron, J. Y. Duquesne, S. Martin, C. Secouard, B. Perrin, *Thin Solid Films* **2013**, *548*, 366.
[77] A. Sharafi, C. G. Haslam, R. D. Kerns, J. Wolfenstine, J. Sakamoto, *J. Mater. Chem. A* **2017**, *5*, 21491.
[78] Z. Zhang, A. R. Gonzalez, K. L. Choy, *ACS Appl. Energy Mater.* **2019**, *2*, 7438.
[79] C. Wang, K. Fu, S. P. Kammampata, D. W. McOwen, A. J. Samson, L. Zhang, G. T. Hitz, A. M. Nolan, E. D. Wachsman, Y. Mo, V. Thangadurai, L. Hu, *Chem. Rev.* **2020**, *120*, 4257.
[80] G. Li, M. Li, L. Dong, X. Li, D. Li, *Int. J. Hydrogen Energy* **2014**, *39*, 17466.
[81] G. Li, M. Li, L. Dong, H. Song, L. Dong, J. Deng, D. Li, *Int. J. Hydrogen Energy* **2014**, *39*, 16103.
[82] L. Zhang, L. Fu, W. Qin, Y. He, H. Liu, H. Hu, *Phys. Chem. Chem. Phys.* **2023**, *25*, 18297.
[83] Z. Zhang, R. G. Antonio, K. L. Choy, *J. Power Sources* **2019**, *435*, 226736.
[84] F. Yang, Q. Liu, W. Xie, P. Xie, J. Shang, X. Shu, *Polymers* **2022**, *14*, 1274.
[85] H. Jiang, Y. Wu, J. Ma, Y. Liu, L. Wang, X. Yao, H. Xiang, *J. Membr. Sci.* **2021**, *640*, 119840.
[86] X. Hu, X. Cheng, S. Qin, G. Yan, J. Malzbender, W. Qiang, B. Huang, *Ceram. Int.* **2018**, *44*, 1902.
[87] X. Hu, W. Qiang, B. Huang, *J. Am. Ceram. Soc.* **2017**, *100*, 4153.
[88] X. Cheng, Y. Li, G. Zhao, W. Qiang, B. Huang, *Ceram. Int.* **2022**, *48*, 27849.
[89] X. Hu, W. Qiang, B. Huang, *Energy Storage Mater.* **2017**, *8*, 141.

© 2024 The Author(s). Advanced Energy Materials published by Wiley-VCH GmbH

[90] M. Qu, W. H. Woodford, J. M. Maloney, W. C. Carter, Y. M. Chiang, K. J. Van Vliet, *Adv. Energy Mater.* **2012**, *2*, 940.
[91] Y. Luo, W. Feng, Z. Meng, Y. Wang, X. Jiang, Z. Xue, *Electrochim. Acta* **2021**, *397*, 139285.
[92] S. Pathak, D. Steinmetz, J. Kuebler, E. Andrew Payzant, N. Orlovskaya, *Ceram. Int.* **2009**, *35*, 1235.
[93] M. Dixit, N. Muralidharan, A. Parejiya, C. Jafta, Z. Du, S. M. Neumayer, R. Essehli, R. Amin, M. Balasubramanian, I. Belharouak, *ACS Appl. Mater. Interfaces* **2022**, *14*, 44292.
[94] S. Guo, Y. Su, K. Yan, C. Zhao, Y. Lu, H. Wang, J. Dong, N. Li, Y. Liu, Y. Guan, F. Wu, L. Chen, *Adv. Sci.* **2024**, *11*, 2404307.
[95] J. Zhang, T. Huang, A. Yu, *J. Power Sources* **2015**, *273*, 894.
[96] J. S. Terreblanche, D. L. Thompson, I. M. Aldous, J. Hartley, A. P. Abbott, K. S. Ryder, *J. Phys. Chem. C* **2020**, *124*, 14622.
[97] M. Yoo, C. W. Frank, S. Mori, S. Yamaguchi, *Polymer* **2003**, *44*, 4197.
[98] H. Pan, Z. Xu, Z. Wei, X. Liu, M. Xu, C. Zong, W. Li, G. Cui, L. Cao, Q. Wang, *ACS Appl. Mater. Interfaces* **2022**, *14*, 33315.
[99] H. A. Hoang, D. Kim, *Chem. Eng. J.* **2022**, *435*, 135092.
[100] X. Huang, S. Huang, T. Wang, L. Zhong, D. Han, M. Xiao, S. Wang, Y. Meng, *Adv. Funct. Mater.* **2023**, *33*, 2300683.
[101] X. Su, K. Guo, T. Ma, P. A. Tamirisa, H. Ye, H. Gao, B. W. Sheldon, *ACS Energy Lett.* **2017**, *2*, 1729.
[102] W. Jiang, L. Yan, X. Zeng, X. Meng, R. Huang, X. Zhu, M. Ling, C. Liang, *ACS Appl. Mater. Interfaces* **2020**, *12*, 54876.
[103] M. Wang, J. Sakamoto, *J. Power Sources* **2018**, *377*, 7.
[104] X. Gu, D. B. Knorr, G. Wang, R. M. Overney, *Thin Solid Films* **2012**, *520*, 1872.
[105] Q. D. Nguyen, K. H. Chung, *Appl. Phys. Lett.* **2020**, *116*, 061604.
[106] H. Li, M. W. Rutland, M. Watanabe, R. Atkin, *Faraday Discuss.* **2017**, *199*, 311.
[107] D. Yoon, N. Mulay, J. Baltazar, D. K. Cao, V. Perez, J. Nelson Weker, M. H. Lee, R. D. Miller, D. Oh, S.-J. J. Lee, *ACS Appl. Energy Mater.* **2023**, *6*, 9400.
[108] S. Patra, M. Yeddala, P. Daga, T. N. Narayanan, *Macromol. Chem. Phys.* **2019**, *220*, 1900348.
[109] L. Albero Blanquer, F. Marchini, J. R. Seitz, N. Daher, F. Bétermier, J. Huang, C. Gervillié, J. M. Tarascon, *Nat. Commun.* **2022**, *13*, 1153.
[110] Q. Liu, Z. Yu, Q. Zhuang, J. K. Kim, F. Kang, B. Zhang, *Adv. Mater.* **2023**, *35*, 2300498.
[111] J. Gu, Z. Liang, J. Shi, Y. Yang, *Adv. Energy Mater.* **2022**, *13*, 2203153.
[112] Y. Bae Song, H. Kwak, W. Cho, K. S. Kim, Y. Seok Jung, K. H. Park, *Curr. Opin. Solid State Mater. Sci.* **2022**, *26*, 100977.
[113] J. Wang, F. Hao, *Energies* **2023**, *16*, 1180.
[114] Y. Sun, O. Gorobstov, L. Mu, D. Weinstock, R. Bouck, W. Cha, N. Bouklas, F. Lin, A. Singer, *Nano Lett.* **2021**, *21*, 4570.
[115] R. Sandt, Y. Wang, R. Spatschek, *Solid State Ionics* **2023**, *402*, 116364.
[116] S. Yu, R. D. Schmidt, R. Garcia-Mendez, E. Herbert, N. J. Dudney, J. B. Wolfenstine, J. Sakamoto, D. J. Siegel, *Chem. Mater.* **2015**, *28*, 197.
[117] Y. Ren, C. Sun, J. Liu, G. Cai, X. Tan, C. Zhang, *Mater. Today Commun.* **2022**, *33*, 104570.
[118] Z. Wang, Y. Jing, Y. Sun, W. Li, J. Yang, X. Li, *Comput. Mater. Sci.* **2024**, *235*, 112824.
[119] H. Chen, T. Hong, Y. Jing, *J. Alloys Compd.* **2020**, *819*, 152950.
[120] J. Zhang, G. Zhu, H. Li, J. Ju, J. Gu, R. Xu, S. Jin, J. Zhou, B. Chen, *Nano Res.* **2022**, *16*, 3516.
[121] S. Xiong, X. Xu, X. Jiao, Y. Wang, O. O. Kapitanova, Z. Song, Y. Liu, *Adv. Energy Mater.* **2023**, *13*, 2203614.
[122] J. Tippens, J. C. Miers, A. Afshar, J. A. Lewis, F. J. Q. Cortes, H. Qiao, T. S. Marchese, C. V. Di Leo, C. Saldana, M. T. McDowell, *ACS Energy Lett.* **2019**, *4*, 1475.
[123] S. Monismith, C. D. Fincher, Y. M. Chiang, J. Qu, R. Dingreville, *Adv. Energy Mater.* **2023**, *14*, 2303567.
[124] R. Mücke, N. Yaqoob, M. Finsterbusch, F. Al-Jaljouli, P. Kaghazchi, D. Fattakhova-Rohlfing, O. Guillon, *J. Mater. Chem. A* **2023**, *11*, 18801.
[125] G. Bucci, T. Swamy, Y. M. Chiang, W. C. Carter, *J. Mater. Chem. A* **2017**, *5*, 19422.
[126] Y. Kim, H. Jo, J. L. Allen, H. Choe, J. Wolfenstine, J. Sakamoto, G. Pharr, *J. Am. Ceram. Soc.* **2016**, *99*, 1367.
[127] R. Xu, F. Liu, Y. Ye, H. Chen, R. R. Yang, Y. Ma, W. Huang, J. Wan, Y. Cui, *Adv. Mater.* **2021**, *33*, 2104009.
[128] Y. Yang, Q. Wu, Y. Cui, Y. Chen, S. Shi, R. Z. Wang, H. Yan, *ACS Appl. Mater. Interfaces* **2016**, *8*, 25229.
[129] Z. W. Zhi Deng, I.-H. Chu, J. Luo, S. P. Ong, *J. Electrochem. Soc.* **2016**, *163*, A67.
[130] M. Munsif, M. Shah, Z. Ullah, M. W. Ashraf, M. Fayaz, H. A. Alsalmah, G. Murtaza, *Phys. B* **2023**, *661*, 414932.
[131] W. Qin, Q. Yang, Y. He, L. Zhang, H. Hu, *Mech. Mater.* **2023**, *185*, 104773.
[132] C. Xin, K. Wen, S. Guan, C. Xue, X. Wu, L. Li, C. W. Nan, *Front. Mater.* **2022**, *9*, 864478.
[133] M. Nowicki, A. Richter, B. Wolf, H. Kaczmarek, *Polymer* **2003**, *44*, 6599.
[134] D. Shore, J. C. Avelar-Batista Wilson, A. Matthews, A. Yerokhin, *Surf. Coat. Technol.* **2021**, *428*, 127898.
[135] J. Djokic, A. Kojovic, D. Stojanovic, A. Marinkovic, G. Vukovic, R. Aleksic, P. Uskokovic, *J. Serb. Chem. Soc.* **2012**, *77*, 1723.
[136] L. Tsou, J. A. Sauer, M. Hara, *J. Polym. Sci., Part B: Polym. Phys.* **2000**, *38*, 1377.
[137] X. Xu, H. Wang, L. Jiang, X. Wang, S. A. Payne, J. Y. Zhu, R. Li, *Macromolecules* **2014**, *47*, 3409.
[138] A. Masias, N. Felten, R. Garcia-Mendez, J. Wolfenstine, J. Sakamoto, *J. Mater. Sci.* **2018**, *54*, 2585.
[139] C. D. Fincher, D. Ojeda, Y. Zhang, G. M. Pharr, M. Pharr, *Acta Mater.* **2020**, *186*, 215.
[140] L. S. d. Vasconcelos, R. Xu, J. Li, K. Zhao, *Extreme Mech. Lett.* **2016**, *9*, 495.
[141] K. Min, E. Cho, *Phys. Chem. Chem. Phys.* **2018**, *20*, 9045.
[142] N. Sharma, D. Meng, X. Wu, L. S. de Vasconcelos, L. Li, K. Zhao, *Extreme Mech. Lett.* **2023**, *58*, 101920.
[143] W. Mao, X. Zhu, Z. Zhang, H. Huang, C. Dai, J. Pan, Y. Pan, X. Chen, D. Fang, *Mater. Sci. Eng., A* **2020**, *781*, 139223.
[144] E. J. Cheng, N. J. Taylor, J. Wolfenstine, J. Sakamoto, *J. Asian Ceram. Soc.* **2018**, *5*, 113.
[145] A. B. Kanagaraj, P. Chaturvedi, T. S. Alkindi, R. A. Susantyoko, B. H. An, S. P. Patole, K. Shanmugam, S. AlMheiri, S. AlDahmani, H. AlFadaq, D. S. Choi, *Mater. Lett.* **2018**, *230*, 57.
[146] D. E. Demirocak, B. Bhushan, *J. Power Sources* **2015**, *280*, 256.
[147] S. Ramdon, B. Bhushan, *J. Power Sources* **2014**, *246*, 219.
[148] C. Schwalb, P. Frank, S. Hummel, J. Sattelkov, R. Winkler, J. Huetner, O. Domanov, G. Fantner, H. Plank, *Microsc. Microanal.* **2020**, *26*, 1800.
[149] S. Hummel, K. Elibol, D. Zhang, K. Sampathkumar, O. Frank, D. Eder, C. Schwalb, J. Kotakoski, J. C. Meyer, B. C. Bayer, *Appl. Phys. Lett.* **2021**, 118.
[150] G. H. Wu, P. G. Mitchell, J. G. Galaz-Montoya, C. W. Hecksel, E. M. Sontag, V. Gangadharan, J. Marshman, D. Mankus, M. E. Bisher, A. K. R. Lytton-Jean, J. Frydman, K. Czymmek, W. Chiu, *Structure* **2020**, *28*, 1231.

© 2024 The Author(s). Advanced Energy Materials published by Wiley-VCH GmbH



Shuai Hao is an associate researcher (associate research fellow) at the Institute of New Energy Material Chemistry, Nankai University. Prior to joining Nankai, she worked as a research associate at Faraday Institution and University College London in the UK, after receiving a PhD degree at the Institute of Physics, Chinese Academy of Sciences. Her main research interests are advanced characterizations, including 3D imaging, and their applications in the energy storage field.



Zhaoxiang Wang is a professor at the Institute of Physics, Chinese Academy of Sciences. He worked as a post-doctoral research fellow in Mie University (Japan), University of St. Andrews (UK), and University of Michigan (USA), successively after receiving his PhD degree at the Institute in 1998. He returned to the Institute in 2000 and has been working on materials and devices for the advanced secondary batteries ever since.



Xue-Ping Gao is a Professor at the Institute of New Energy Material Chemistry, Nankai University of China. He received his doctorate in the Department of Chemistry from Nankai University in 1995. He used to work as a visiting research fellow at Kogakuin University in Japan from 1997 to 1999. Currently, his main research is focused on energy storage materials for power sources, including Li–S batteries and Li-ion batteries.



Paul Shearing is a Professor of Sustainable Energy Engineering at the Department of Engineering Science and Director of the ZERO Institute at Oxford University. He holds the Royal Academy of Engineering Chair in Emerging Battery Technologies. His research interests center on the characterization and understanding of materials for batteries and other energy applications with a major focus on the development of new X-ray techniques. He was a founding investigator of The Faraday Institution, the UK's independent institute for electrochemical energy storage research where he leads the LiSTAR and Safebatt research programs.

© 2024 The Author(s). Advanced Energy Materials published by Wiley-VCH GmbH